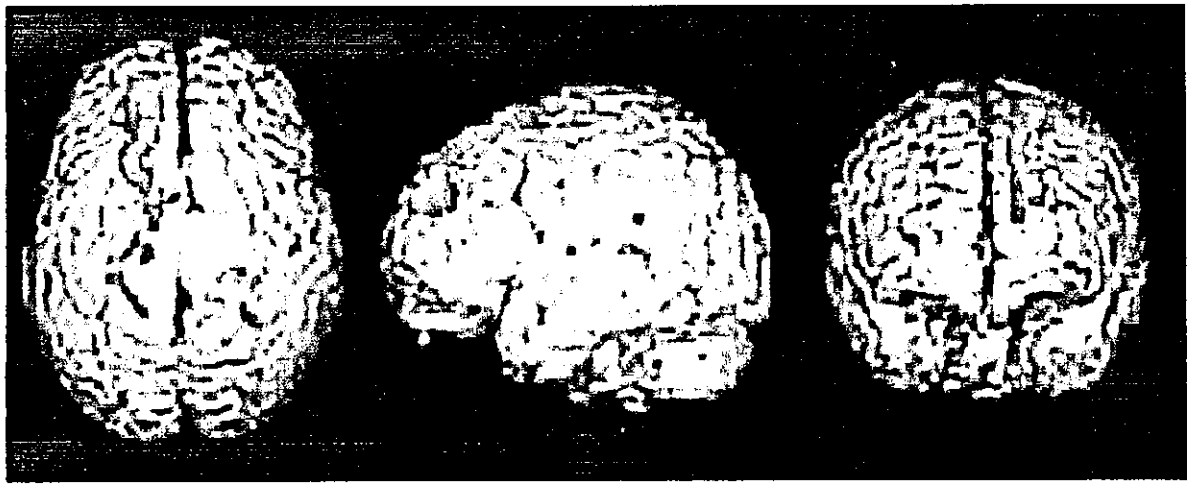

FIG. 1. Significantly different regions ($P < 0.01$, corrected) of relative regional cerebral metabolic rate for glucose (rrCMRglc) with group comparison study. Compared to patients with no visual hallucinations, an increase of rrCMRglc is observed in the left superior frontal gyrus in patients with visual hallucinations.

Normal Controls versus PD

The pattern of decreased and increased rrCMRglc in N-VH and VH, compared to normal controls, was similar, except for frontal areas. The decrease of rrCMRglc seen in both PD groups in the occipital and parietal areas is consistent with previous FDG studies.[17–20] The increase of rrCMRglc in cerebellum and precentral gyrus is consistent with previous reports, indicating that the glucose metabolism in these areas was preserved in nondemented PD patients.[18,19]

N-VH versus VH

The rrCMRglc tended to be greater in the frontal areas in VH compared to N-VH, and the increase reached a significant level in the left superior frontal gyrus. The

TABLE 3. *Peak coordinates in SPM analyses of rrCMRglc*

	Cluster level		Voxel level				
	P corrected	k	*x*	*y*	*z*	T	Regions
NC > N-VH	<0.001	9078	−4	−48	40	7.10	lt PCu/GC (BA 7/31)
			−20	−92	−6	5.64	lt GL (BA 18/17)
	<0.001	7575	44	32	34	6.49	rt GFm (BA 9)
			54	32	10	4.75	rt GFm((BA 46)
	<0.001	2702	56	−38	−10	5.34	rt GTi (BA 20/37)
			58	−32	6	3.50	rt GTm (BA 21)
	<0.001	3599	−52	−30	−6	4.90	lt GTm/GTi (BA 20/37)
			−54	−60	−26	4.01	lt GTi (BA 37)
NC > VH	<0.001	19072	−2	−88	−10	7.53	lt GL (BA 18/17)
			64	−22	34	6.39	rt LPi (BA 40)
NC < N-VH	0.002	1692	12	−56	−32	6.51	rt dentate nucleus
			10	−36	−32	4.99	rt vestibular nucleus
NC < VH	<0.001	2182	−24	−54	−42	5.30	lt dentate nucleus
			−10	−40	−32	3.67	lt vestibular nucleus
	0.001	1874	12	−12	60	5.27	rt GFs (BA 6/4)
			10	−40	68	4.40	rt GPoC (BA 3/1/2)
	0.001	1751	−14	−36	66	4.65	lt GPoC (BA 3/1/2)
			−24	−22	72	4.17	lt GPrC (BA6/4)
N-VH < VH	0.030	1113	−24	20	60	4.45	lt GFs (BA 6/8)
			−16	46	38	4.11	lt GFs (BA 8/9)

Maximum peak coordinate for each anatomical region is listed. Abbreviations: lt, left; rt, right; BA, Brodmann area; PCu, precuneus; GC, cingulate gyrus; GFs, superior frontal gyrus; GFm, middle frontal gyrus; GTm, middle temporal gyrus; GTi, inferior temporal gyrus; GL, lingual gyrus; LPi, inferior parietal lobe; GPoC, postcentral gyrus; GPrC, precentral gyrus; SPM, statistical parametric mapping; rr CMRglc; relative regional cerebral metabolic rate for glucose; N-VH, no visual hallucinations; VH, visual hallucinations.

TABLE 4. *Region of interest analyses of rrCMRglc*

	N-VH	VH	*P*
Dorsolateral prefrontal cortex			
lt	0.87 ± 0.03	0.93 ± 0.08	0.02
rt	0.87 ± 0.04	0.92 ± 0.08	0.07
Primary visual cortex			
lt	0.76 ± 0.06	0.76 ± 0.07	0.98
rt	0.75 ± 0.06	0.76 ± 0.07	0.91
Occipital association cortex			
lt	0.90 ± 0.07	0.89 ± 0.10	0.89
rt	0.88 ± 0.07	0.86 ± 0.08	0.68
Primary motor cortex			
lt	1.01 ± 0.08	1.02 ± 0.05	0.94
rt	1.02 ± 0.09	1.03 ± 0.04	0.79

P values of simple *t* test are listed in the rightmost column. rrCMRglc, relative regional cerebral metabolic rate for glucose; lt, left; rt, right; N-VH, no visual hallucinations; VH, visual hallucinations.

prefrontal regions, including BA 8/9 are implicated in working memory[21,22] and executive cognitive function.[23] In addition to this, primate studies indicated that the prefrontal cortex plays a role in exerting executive control of memory retrieval from the site of long-term storage.[24,25] The occipital and occipitotemporal areas are considered as visual areas.[26,27]

A previous ^{99m}Tc-labeled hexamethyl propyleneamine oxime SPECT study indicated that hallucinatory patients showed significantly lower semiquantitative cerebral blood flow in the left temporal and upper temporo-occipital regions than nonhallucinatory patients.[7] The discrepancy between their and our results might be attributed to three aspects as follows: (1) the difference between cerebral blood flow and glucose metabolism, (2) the difference between medication-induced visual hallucinations and visual hallucinations that persist even after drug reductions, or (3) if demented-patients were included or not.

A previous study of patients with ischemic infarction showed that positive spontaneous visual phenomena (PSVP) were observed in patients with relatively small lesions limited to posterior regions and that larger lesions destroying anteriorly located visual association areas precluded the development of PSVP.[28] A functional MRI study while subjects thought of missing last words of a sentence comparing normal subjects with schizophrenia patients showed that there were no significant group differences in regional brain responses. However, the correlation coefficients between left temporal cortex and left dorsolateral prefrontal cortex were significantly lower in the schizophrenic group and were negatively correlated with the severity of auditory hallucination.[29] Thus, imbalance of activity between primary sensory regions and anterior associative regions, including dorsolateral prefrontal cortex may play a part in PSVP or auditory hallucination. Another study concluded that visual pathway lesions impair visual input and may result in hallucinations from defective visual processing or an abnormal cortical release phenomenon.[30] Our finding may be consistent with this theory.

CONCLUSION

Using FDG PET, group comparison studies were performed to determine the specific regions of the brain that are related to visual hallucinations in PD patients. The pattern of relative hypermetabolism in the frontal cortex with relative hypometabolism in the posterior areas is likely a metabolic feature of visual hallucinations in PD patients. The mechanism of hallucination is unknown, and more studies need to be conducted.

Acknowledgments: We thank Dr. Alain Dagher, Montreal Neurological Institute, McGill University, for reading this report and providing thoughtful remarks. This study was supported by funds for Research on Longevity Science and for Comprehensive Research of Aging and Health from the Ministry and Welfare of Japan.

REFERENCES

1. Korczeyn AD. Hallucinations in Parkinson's disease. Lancet 2001; 358:1031–1032.
2. Barnes J, David S. Visual hallucinations in Parkinson's disease: a review and phenomenological survey. J Neurol Neurosurg Psychiatry 2001;70:727–733.
3. Sanchez-Ramos JR, Ortoll R, Paulson GW. Visual hallucinations associated with Parkinson disease. Arch Neurol 1996;53:1265–1268.
4. Fenelon G, Mahieux F, Huon R, Ziegler M. Hallucinations in Parkinson's disease: prevalence, phenomenology and risk factors. Brain 2000;123:733–745.
5. Holroyd S, Currie L, Wooten GF. Prospective study of hallucinations and delusions in Parkinson's disease. J Neurol Neurosurg Psychiatry 2001;70:734–738.
6. Goetz CG, Leurgans S, Pappert EJ, Raman R, Stemer AB. Prospective longitudinal assessment of hallucinations in Parkinson's disease. Neurology 2001;57:2078–2082.
7. Okada K, Suyama N, Oguro H, Yamaguchi S, Kobayashi S. Medication-induced hallucination and cerebral blood flow in Parkinson's disease. J Neurol 1999;246:365–368.
8. Friston KJ, Holmes AP, Worsley KJ, Poline JP, Frith CD, Frackowiak RSJ. Statistical parametric maps in functional imaging: a general linear approach. Hum Brain Mapp 1995;2:189–210.
9. Calne DB, Snow BJ, Lee C. Criteria for diagnosing Parkinson's disease. Ann Neurol 1992;32(Suppl.):S125–S127.
10. McKeith IG, Galasko D, Kosaka K, et al. Consensus guidelines for the clinical and pathologic diagnosis of dementia with Lewy bodies (DLB): report of the consortium on DLB international workshop. Neurology 1996;47:1113–1124.
11. Folstein MF, Folstein SE, McHugh PR. "Mini-mental state". A practical method for grading the cognitive state of patients for the clinician. J Psychiatr Res 1975;12:189–198.
12. Hoehn MM, Yahr MD. Parkinsonism: onset, progression and mortality. Neurology 1967;17:427–442.
13. OgawaT. Selection and change of dopamine agonist. In: Yanagisawa N, editor. Parkinson's disease—diagnosis and treatment. Tokyo: Kinbara-shoten; 2000. p 180–188.

14. Wang GJ, Volkow ND, Wolf AP, Brodie JD, Hitzemann RJ. Intersubject variability of brain glucose metabolic measurements in young normal males. J Nucl Med 1994;35:1457–1466.
15. Arahata Y, Hirayama M, Ieda T, et al. Parieto-occipital glucose hypometabolism in Parkinson's disease with autonomic failure. J Neurol Sci 1999;163:119–126.
16. Hutchins GD, Holden JE, Koeppe RA, Halama JR, Gatley SJ, Nickles RJ. Alternative approach to single-scan estimation of cerebral glucose metabolic rate using glucose analogs, with particular application to ischemia. J Cereb Blood Flow Metab 1984; 4:35–40.
17. Eberling JL, Richardson BC, Reed BR, Wolfe N, Jagust WJ. Cortical glucose metabolism in Parkinson's disease without dementia. Neurobiol Aging 1994;15:329–335.
18. Bohnen NI, Minoshima S, Giordani B, Frey KA, Kuhl DE. Motor correlates of occipital glucose hypometabolism in Parkinson's disease without dementia. Neurology 1999;52:541–546.
19. Hu MTM, Taylor-Robinson SD, Chaudhuri KR, et al. Cortical dysfunction in non-demented Parkinson's disease patients: a combined (31)P-MRS and (18)FDG-PET study. Brain 2000;123:340–352.
20. Mentis MJ, McIntoshi AR, Perrine K, et al. Relationships among the metabolic patterns that correlate with mnemonic, visuospatial, and mood symptoms in Parkinson's disease. Am J Psychiatry 2002;159:746–754.
21. Goldman-Rakic PS. Cellular basis of working memory. Neuron 1995;14:477–485.
22. Cabeza R, Nyberg L. Imaging cognition II: an empirical review of 275 PET and fMRI studies. J Cogn Neurosci 2000;12:1–47.
23. MacDonald AW III, Cohen JD, Stenger VA, Carter CS. Dissociating the role of the dorsolateral prefrontal and anterior cingulate cortex in cognitive control. Science 2000;288:1835–1838.
24. Hasegawa I, Fukushima T, Ihara T, Miyashita Y. Callosal window between prefrontal cortices: cognitive interaction to retrieve long-term memory. Science 1998;281:814–818.
25. Tomita H, Ohbayashi M, Nakahara K, Hasegawa I, Miyashita Y. Top-down signal from prefrontal cortex in executive control of memory retrieval. Nature 1999;401:699–703.
26. Kretshmann HJ, Weinirich W. Visual systems. In: Cranial neuroimaging and clinical neuroanatomy. New York: Thieme; 1992. p 289–299.
27. Roland PE. The posterior division of the brain: the parietal, temporal, and occipital cortices. In: Brain activation. New York: Wiley-Liss; 1993. p 365–393.
28. Vaphiades MS, Celesia GG, Brigell MG. Positive spontaneous visual phenomena limited to the hemianopic field in lesions of central visual pathways. Neurology 1996;47:408–417.
29. Lawrie SM, Buechel C, Whalley HC, Frith CD, Friston KJ, Johnston EC. Reduced frontotemporal functional connectivity in schizophrenia associated with auditory hallucinations. Biol Psychiatry 2002;51:1008–1001.
30. Manford M, Andermann F. Complex visual hallucinations. Clinical and neurobiological insights. Brain 1998;121:1819–1840.

Cerebral atrophy and its relation to cognitive impairment in Parkinson disease

A. Nagano-Saito, MD, PhD; Y. Washimi, MD, PhD; Y. Arahata, MD, PhD; T. Kachi, MD, PhD; J.P. Lerch, BA; A.C. Evans, PhD; A. Dagher, MD; and K. Ito, MD, PhD

Abstract—*Objective:* Voxel-based morphometry was used to compare the amounts of gray matter in the brains of patients with Parkinson disease (PD) and normal control subjects (NCs) and to identify the specific regions responsible for cognitive dysfunction in PD. *Methods:* Patients were classified into nondemented (ND) and demented (D) groups according to the criteria of the Diagnostic and Statistical Manual of Mental Disorders (4th ed.), and a group comparison was performed. In the ND patients, a correlation was also performed between local gray matter density and the score on Raven Colored Progressive Matrices (RCPM), a test of executive and visuospatial function. *Results:* In patients with advanced ND-PD vs NCs, atrophic changes were observed in the limbic/paralimbic areas and the prefrontal cortex. In D vs ND patients, atrophic change was observed widely in the limbic/paralimbic system, including the anterior cingulate gyrus and hippocampus as well as the temporal lobe, dorsolateral prefrontal cortex, thalamus, and caudate nucleus. The RCPM score was positively correlated with the gray matter density in the dorsolateral prefrontal cortex and the parahippocampal gyrus. *Conclusions:* In patients with Parkinson disease (PD), atrophic changes occur mainly in the limbic/paralimbic and prefrontal areas. These atrophic changes may be related to the development of dementia in PD.

NEUROLOGY 2005;64:224–229

Cognitive impairment is relatively frequent in Parkinson disease (PD), especially at an advanced stage. In its severe form, it may be global and meet the Diagnostic and Statistical Manual of Mental Disorders (4th ed.; DSM- IV) criteria for dementia.[1] The prevalence of dementia in PD is estimated to be 20 to 40%.[1,2] Moreover, even in the absence of dementia, specific impairments in executive function, visual memory, and visuospatial abilities are often present.[3,4] Raven Colored Progressive Matrices (RCPM), which was initially developed as a nonverbal intellectual test,[5] has been shown to be sensitive to cognitive deficits in PD[6] and can be considered to rely on at least two cognitive factors: visuospatial and executive functions.[7]

A small number of MRI studies have related brain atrophy to cognitive dysfunction in PD. There have been reports, among nondemented PD (ND-PD) patients, of major correlations between verbal learning or frontal lobe function scores and ventricular enlargement[8] and between annual reductions in brain volume and reductions in performance and full-scale IQ.[9] In another study of ND-PD patients, hippocampal atrophy was found to correlate with memory impairment.[10] Finally, reduced gray matter volume in demented PD (D-PD) patients was observed in widespread cortical (temporal, occipital, lateral prefrontal) and subcortical (caudate, putamen, thalamus) areas vs control subjects using voxel-based morphometry (VBM).[11] However, as far as we know, there have been no reports on the relation between gray matter atrophy and cognitive impairment in ND-PD using VBM.

The aim of this study was to identify the gray matter atrophic changes that are associated with specific cognitive impairment and dementia in PD. We used VBM to assess focal brain atrophy in the whole brain of PD patients with and without dementia and matched healthy control subjects. We also correlated gray matter density to performance on the RCPM in the ND-PD patients.

Methods. *Subjects.* Fifty-eight patients with PD who fulfilled the clinical criteria for the diagnosis of PD[12] were recruited. Detailed interview with patients and their families and neurologic examination were used to determine cognitive status. Nine patients were diagnosed as D-PD according to the DSM-IV criteria. All of them had impairments in memory function affecting their daily life and had experienced visual hallucinations. One patient had cognitive fluctuation and, as a result, also fulfilled the criteria of the Consortium on Dementia with Lewy Bodies International Workshop.[13] In all D-PD, the onset of parkinsonism preceded the development of dementia by at least 2 years, and significant cognitive impairment involving executive function and/or visuospatial abilities preceded the memory difficulties. Among the

From Department of Neurology (Drs. Nagano-Saito, Washimi, Arahata, and Kachi), National Hospital for Geriatric Medicine, and Department of Brain Science and Molecular Imaging (Dr. Ito), National Institute for Longevity Sciences, National Center for Geriatrics and Gerontology, Obu, Japan; and McConnell Brain Imaging Centre (Drs. Nagano-Saito, Lerch, Evans, and Dagher), Montreal Neurological Institute, McGill University, Montreal, Quebec, Canada.

Supported by funds for Research on Health Science of Mind of Aging and Health from the Ministry and Welfare of Japan.

Received May 20, 2004. Accepted in final form September 29, 2004.

Address correspondence and reprint requests to Dr. Y. Arahata, Department of Neurology, National Center for Geriatrics and Gerontology, 36-3 Gengo, Morioka, Obu, Aichi, Japan 474-8511; e-mail: arahatay@nils.go.jp

Table 1 Clinical features of normal subjects and patients

Group category	Comparison	No.	Age, y	H-Y Scale	UPDRS motor score	Disease duration, y	MMSE score
NC	NC vs all ND-PD NC vs advanced ND-PD	31	63.5 ± 8.8				29.2 ± 1.2
ND-PD	NC vs all ND-PD	39	61.8 ± 8.1	2.3 ± 0.9	25.5 ± 16.1	3.5 ± 3.4	28.4 ± 1.9
	NC vs advanced ND-PD	19	62.6 ± 7.9	3.1 ± 0.5	37.4 ± 15.3	4.9 ± 4.3	28.1 ± 2.0
	Advanced ND-PD vs D-PD	17	65.4 ± 6.4	3.1 ± 0.6	38.7 ± 15.7	5.2 ± 4.5	27.9 ± 2.0
	Regression analysis	38	61.9 ± 8.2	2.3 ± 0.9	26.0 ± 16.0	3.6 ± 3.4	28.4 ± 1.9
D-PD	ND-PD vs D-PD	9	67.3 ± 5.4	3.3 ± 0.7	45.7 ± 10.9*	9.3 ± 5.4	16.1 ± 5.7

* n = 6.

H-Y = Hoehn and Yahr; UPDRS = Unified Parkinson's Disease Rating Scale; MMSE = Mini-Mental State Examination; NC = normal control; ND-PD = nondemented Parkinson disease; D-PD = demented Parkinson disease.

remaining PD patients, none fulfilled the DSM-IV criteria for delirium or amnesic disorder. After excluding patients with a history of hallucination, severe depression, severe autonomic failure, or resistance to dopaminergic medications, 39 PD patients remained to form the ND-PD group. All patients were rated using the Hoehn and Yahr (H-Y) Scale and the Mini-Mental State Examination (MMSE). All patients except three D-PD patients were rated using the Unified Parkinson's Disease Rating Scale (UPDRS), and all ND-PD patients except one underwent the RCPM Test. Thirty-one normal control subjects (NCs), who were neurologically intact and age matched to the ND-PD patients, were also recruited. Permission to perform these studies was obtained from the Ethical Committee of the National Center for Geriatrics and Gerontology.

MRI and VBM. High-resolution volumetric MRI was performed on a 1.5 T Visart MRI scanner (Toshiba, Tokyo, Japan) using a three-dimensional field echo sequence (repetition time 20 milliseconds, echo time 7 milliseconds, flip angle 35°), generating T1-weighted contiguous sagittal slices with a pixel size of 0.89 × 0.89 mm and a slice thickness of 1.3 mm. These T1-weighted brain volumes were linearly transformed into stereotaxic space using nine parameters[14] to match the Montreal Neurologic Institute template with a voxel size of 1 × 1 × 1 mm. The volumes also underwent a nonuniformity correction[15] to remove variations in signal intensity related to radiofrequency inhomogeneity. With use of the individual parameters of the linear transformation, the images were transformed into the standardized stereotaxic space. The transformed images were then classified into gray matter, white matter, and CSF using an automatic tissue classification algorithm.[16] Mask images were generated from the individual spatially transformed images to remove the skull and dura.[17] With use of the tissue-classified and mask images, probability images of gray matter were created using an algorithm that estimates the relative amount of gray and white matter, CSF, and background in each voxel.[18] These gray matter probability images were then blurred with an isotropic Gaussian kernel (full width at half-maximum = 8 mm). Statistical analyses were performed on the blurred gray matter probability images.

Statistical analysis. Four voxel-based statistical analyses were performed as follows: 1) group comparison between 31 NCs and 39 ND-PD patients, 2) group comparison between 31 NCs and 19 advanced ND-PD patients (defined as H-Y score of >2), 3) group comparison between 17 advanced ND-PD and 9 D-PD patients, and 4) regression analysis between the RCPM scores and the gray matter probability maps of 38 ND-PD patients. In the third comparison, patients matched to the D-PD patients for age and H-Y score were selected from the advanced ND-PD group. Because these two groups could not be matched for disease duration, this subtraction was also carried out with disease duration as a confounding covariate.

The effect of each comparison was tested, and the result was indicated as a T map. Random field theory was used to assign a p value to each cluster based on its height and extent.[19] The degrees of freedom for each comparison were set to the number of subject scans used minus 2. Clusters with a height threshold set at $p < 0.001$ and an extent threshold set at corrected $p < 0.05$ were considered significant.

Results. The number, mean age, disease duration, H-Y score, UPDRS motor score, and MMSE score for each group of each comparison are shown in table 1. No significant differences were observed in mean age, H-Y score, or UPDRS motor score in any group comparisons. There was, however, a trend toward longer disease duration in the D-PD group vs the ND-PD group. There were no significant differences in dosages of any antiparkinsonian medication between advanced ND-PD and D-PD groups. The RCPM score ranged from 20 to 36 (mean 30.0 ± 4.4). There was no correlation between the UPDRS motor scores and the RCPM scores in ND-PD patients (correlation coefficient −0.02, $p = 0.93$).

There were no differences in gray matter density between the ND-PD and NC groups. In the advanced ND-PD group vs NCs, there were atrophic changes in the bilateral straight gyrus extending into the subcallosal gyrus, Brodmann area (BA) 11/25, left inferior frontal gyrus (ventrolateral prefrontal cortex, BA 44), and left parahippocampal gyrus (BA 30) (figure 1). In the D-PD group vs matched ND-PD patients, there were atrophic changes in the bilat-

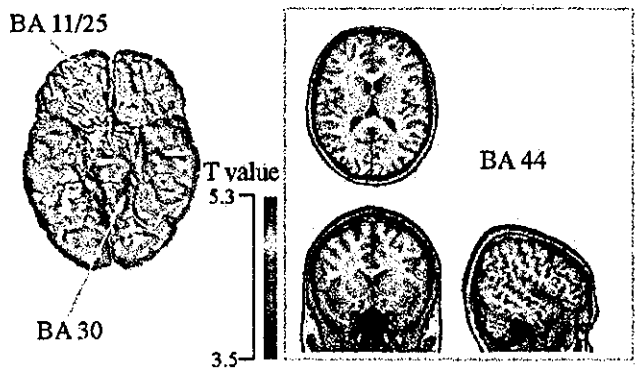

Figure 1. Regions with significant difference between normal control subject and nondemented patient with advanced Parkinson disease. The T value with 3.5 and above is superimposed on the template MRI. The right side of each axial and coronal figure corresponds with the right side of the brain. BA = Brodmann area.

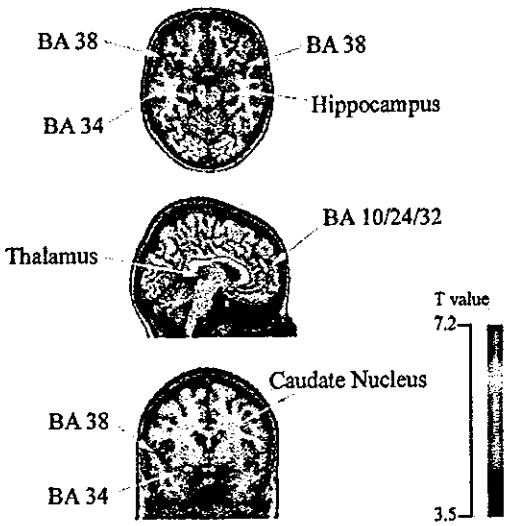

Figure 2. Regions with significant difference between advanced Parkinson disease without dementia and Parkinson disease with dementia. The T value with 3.5 and above is superimposed on the template MRI. The right side of each axial and coronal figure corresponds with the right side of the brain. BA = Brodmann area.

eral anterior cingulate gyrus extending to the medial frontal gyrus (BA 10/24/32), bilateral parahippocampal gyrus (BA 34), bilateral anterior part of the superior temporal gyrus, corresponding to the temporal operculum, extending to the temporal polar region (BA 22/38), right hippocampus, right middle frontal gyrus (dorsolateral prefrontal cortex, BA 46), bilateral caudate nuclei, and left thalamus (figure 2). These results were essentially unaffected when disease duration was covaried out (table 2). In ND-PD patients, the RCPM score was positively correlated with the gray matter density in the right parahippocampal/fusiform gyrus (BA 37), left parahippocampal gyrus (BA 19/28), left superior frontal gyrus (BA 10), and right middle frontal gyrus (dorsolateral prefrontal cortex, BA 9) (figure 3). Table 2 lists the peaks of the most significant differences in these results.

Discussion. *NCs vs ND-PD patients.* In the ND-PD group as a whole, no loss of gray matter was observed vs NC, and this result is consistent with previous MRI studies.[20,21] In contrast, the advanced ND-PD patients showed gray matter loss in three areas vs NCs: straight gyrus, inferior frontal gyrus, and parahippocampal gyrus. The straight gyrus, which is considered to be an extension of the anterior cingulate into the frontal lobe,[22] belongs to the paralimbic system, as does the parahippocampal gyrus. This finding is consistent with pathologic studies showing that the components of the limbic system are particularly vulnerable to degeneration in PD.[23] Mild pathologic change has also been observed in frontal association areas in PD,[23] and the atrophic change in the lateral prefrontal cortex observed in

***Table 2** List of peaks of most significant differences in comparisons*

Comparison	Region	Cluster				Coordinate		
		Voxels	*p* Corrected	Peak *T* value	Peak *T* value*	*x*	*y*	*z*
NC vs PD advanced	L rectal gyrus (BA 11/25)	1,143	<0.001	4.59		0	28	−26
	R inferior frontal gyrus (BA 44)	635	0.001	5.31		52	13	15
	L parahippocampal gyrus (BA 30)	380	0.026	4.3		−13	−40	−6
PD vs D-PD	L medial frontal gyrus (BA 10/24/32)	4,316	<0.001	7.21	6.82	−5	50	13
	L superior temporal gyrus (BA 38/22)	2,761	<0.001	5.34	5.11	−47	20	−18
	L parahippocampal gyrus (BA 34)	1,286	<0.001	6.75	5.84	−24	2	−16
	R caudate nucleus (body/head)	1,211	<0.001	4.82	4.72	12	1	18
	R superior temporal gyrus (BA 38/22)	1,034	<0.001	6.16	5.55	36	9	−17
	L thalamus	705	0.001	4.87	3.45	−7	−27	2
	R hippocampus	524	0.004	5.27	4.57	32	−17	−17
	L caudate nucleus (body/head)	464	0.007	4.39	4.33	−11	0	14
	R middle frontal gyrus (BA 46)	365	0.024	4.39	4.18	42	47	15
PD and RCPM	R parahippocampal/fusiform gyrus (BA 37)	678	0.001	5.01		27	−40	−14
	L superior frontal gyrus (BA 10)	611	0.002	6.07		−25	55	13
	L parahippocampal gyrus (BA 19)	511	0.005	4.63		−30	−56	−2
	R insula	509	0.005	4.74		38	11	2
	R middle frontal gyrus (BA 9)	441	0.011	5.39		45	8	37
	L parahippocampal gyrus (BA 28)	418	0.015	4.02		−22	−13	−14

* Peak *T* value with disease duration covaried out.

NC = normal control; PD = Parkinson disease; D-PD = demented Parkinson disease; RCPM = Raven Colored Progression Matrices; BA = Brodmann area.

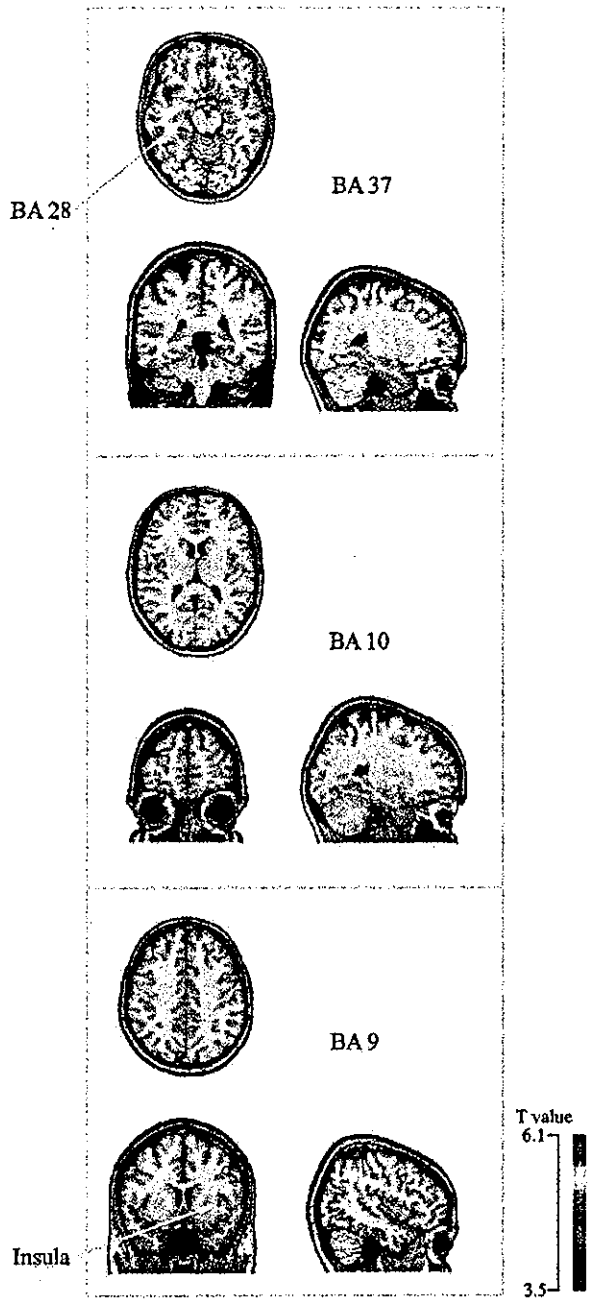

Figure 3. Region with significantly positive correlation to the Raven Colored Progressive Matrices score. The T value with 3.5 and above is superimposed on the template MRI. The right side of each axial and coronal figure corresponds with the right side of the brain. BA = Brodmann area.

our study in advanced PD patients likely reflects intrinsic frontal lobe degeneration.

ND-PD vs D-PD patients. When we compared D-PD patients with a group of ND-PD patients matched for motor disability, we observed widespread atrophic changes in the limbic/paralimbic system. We selected D-PD patients according to the DSM-IV criteria, which require memory impairment. Thus, our finding of atrophy involving the Papez circuit, which is strongly implicated in memory, likely accounts for the memory impairment in our group of D-PD patients. Pathologic studies have implicated the medial temporal lobe in dementia in PD. Demented patients have higher densities of parahippocampal Lewy bodies on pathologic examination,[24] and there have been reports of correlations between clinical dementia severity and the number of Lewy bodies in the entorhinal cortex[25] and the density of Lewy neurites in the CA2 field of the hippocampus.[26] Moreover, previous MRI studies indicated that hippocampal atrophy is related to impaired memory in ND-PD patients.[10,27] We conclude that atrophy of the hippocampus and parahippocampal gyrus may be an important determinant of dementia in PD.

Within the limbic/paralimbic system, the strongest difference in gray matter between the ND-PD and D-PD patients was observed in the anterior cingulate gyrus extending into the medial frontal gyrus. The anterior cingulate cortex is one of the cortical areas showing the greatest concentration of Lewy bodies in PD,[23,24,28] and a significant correlation has been reported between Clinical Dementia Rating Scale score and Lewy body density in this region.[25] Neuroimaging studies have implicated the anterior cingulate gyrus in attention[29] and in a variety of tasks that require high-level cognitive processing.[30] Thus, the loss of gray matter in the anterior cingulate gyrus may be related to the impairment in the ability to spontaneously generate efficient cognitive strategies in patients with PD.[31]

In a previous PET study, we described a decrease in the 6-[^{18}F] fluoro-L-dopa influx rate constant in the anterior cingulate in D-PD vs ND-PD.[32] It is possible that the loss of gray matter in the anterior cingulate described in the current study includes the loss of mesolimbic dopaminergic projections to the area. However, anterior cingulate atrophy would likely also cause partial volume effects that could have accounted for our previous result.

Reduced gray matter density was also observed in the thalamus and caudate in D-PD patients. These subcortical atrophic changes are consistent with a previous pathologic study in D-PD patients[33] and two recent VBM studies.[11,34] Another MRI study reported no caudate atrophy in D-PD patients vs controls[35]; however, the measure used was whole caudate volume rather than gray matter density.

In a recent VBM study, D-PD patients were found to have a pattern of gray matter loss similar to dementia with Lewy bodies but different from Alzheimer disease (AD).[11] D-PD patients and patients with dementia with Lewy bodies both had widespread cortical (temporal, occipital, lateral prefrontal) and subcortical (caudate, putamen, thalamus) atrophy, with relative sparing of the medial temporal structures compared with control subjects and patients with AD. These results are at odds with those presented here. We found atrophy of the medial temporal lobe structures in the D-PD patients, consistent with previous reports in PD and similar to what has been

reported in AD.[27,36] A possible explanation is that our use of the DSM-IV criteria likely weighted our D-PD sample more toward memory impairment. Thus, the pattern of cerebral atrophy in D-PD most likely depends on the clinical characteristics of the patients studied.

There were no significant differences in medication dosages and clinical features, except MMSE scores, between the D-PD and ND-PD groups. However, the disease duration of D-PD tended to be longer than in ND-PD patients, consistent with a previous observation that longer disease duration is a risk factor for dementia in PD.[1,2] Thus, we cannot say whether atrophy of caudate and limbic/paralimbic and prefrontal areas is merely a result of disease progression or a feature specific to the subgroup of PD patients who develop dementia. Nonetheless, our results allow us to identify gray matter loss in these areas as the anatomic substrate of dementia in PD, a notion that is supported by the fact that co-varying out disease duration did not significantly affect the statistical map and also by the regression analysis in ND patients (see below). Finally, it should be noted that in our study, all D-PD patients had experienced visual hallucinations; therefore, our results may not generalize to PD patients with dementia and no hallucinations.

Regression analysis using RCPM score. Performance on the RCPM can be considered to involve both executive and visuospatial function in PD patients.[7] Previous PET activation studies with the Raven Progressive Matrices task (a variation of RCPM) in young healthy subjects showed a task-related increase of regional cerebral blood flow in areas involved in executive (prefrontal cortex) and visuospatial (occipital, parietal, and hippocampal/parahippocampal regions) function.[37] Therefore, our finding of a positive correlation between the RCPM score and gray matter density in the dorsolateral prefrontal cortex provides an explanation for executive dysfunction in PD. Although dopamine loss in the striatum may affect frontal lobe function by disrupting activity within basal ganglia–thalamocortical circuits,[38,39] our finding suggests that intrinsic frontal lobe degeneration may also play a role. We also observed a positive correlation between the RCPM score and gray matter density in the fusiform and parahippocampal gyri. This parahippocampal gyrus peak, which is more posterior than the parahippocampal gyrus peak in the D-PD vs ND-PD comparison, is in an area thought to be involved in the processing of spatial information.[40,41] Thus, atrophic change in the posterior part of the parahippocampal gyrus may lead to impairment of the visuospatial component of the RCPM.

PET activation with a delayed visual discrimination task that shares cognitive features with the RCPM has been reported.[42] In young subjects, the neutral network involved in this task was shown to include the prefrontal cortex (BA 10), fusiform gyrus, parahippocampal gyrus, posterior cingulate (precuneus), and inferior parietal gyrus. On the contrary, in the older subjects, the network included more anterior areas, namely, the caudate nucleus, dorsolateral prefrontal cortex (BA 9/46), and anterior cingulate gyrus (BA 32). Thus, in older subjects, the caudate nucleus is likely important in the RCPM task. However, in PD patients, because of the impairment of nigrostriatal dopaminergic projection, the network for the "young" (prefrontal cortex and fusiform/parahippocampal gyrus) may be recruited. Recruitment of the hippocampus during performance of a task that normally activates the caudate nucleus has previously been described in PD.[38] If such a recruitment is compensatory, damage to prefrontal and medial temporal structures would likely impair performance on the task. Indeed, we observed a significant correlation between the amounts of the gray matter and the RCPM performance in these two regions in our patients with PD.

RCPM performance did not correlate significantly with severity of PD motor symptoms in this current study, as also reported previously.[7] There is controversy regarding the effectiveness of dopamine replacement on cognitive impairment in PD.[43,44] In PD, the combined impairment of the basal ganglia–thalamocortical circuits due to dopamine deficiency and of the prefrontal cortex and parahippocampal gyrus due to gray matter atrophy may account for the lack of effect of dopamine repletion on cognition.

Acknowledgment

The authors thank Sylvain Milot (McConnell Brain Imaging Centre, Montreal Neurologic Institute, Montreal, Quebec, Canada) for technical help with images.

References

1. Giladi N, Treves TA, Paleacu D, et al. Risk factors for dementia, depression and psychosis in long-standing Parkinson's disease. J Neural Transm 2000;107:59–71.
2. Aarsland D, Tandberg E, Larsen JP, Cummings JL. Frequency of dementia in Parkinson disease. Arch Neurol 1996;53:538–542.
3. Dubois B, Pillon B. Cognitive deficits in Parkinson's disease. J Neurol 1997;244:2–8.
4. Janvin C, Aarsland D, Larsen JP, Hugdahl K. Neuropsychological profile of patients with Parkinson's disease without dementia. Dement Geriatr Cogn Disord 2003;15:126–131.
5. Raven JC. Standard Progressive Matrices: set A, A_B, B. London: Lewis, 1962.
6. Farina E, Gattellaro G, Pomati S, et al. Researching a differential impairment of frontal functions and explicit memory in early Parkinson's disease. Eur J Neurol 2000;7:259–267.
7. Cronin-Golomb A, Braun AE. Visuospatial dysfunction and problem solving in Parkinson's disease. Neuropsychology 1997;11:44–52.
8. Alegret M, Junque C, Pueyo R, et al. MRI atrophy parameters related to cognitive and motor impairment in Parkinson's disease. Neurologia 2001;16:63–69.
9. Hu MT, White SJ, Chaudhuri KR, Morris RG, Bydder GM, Brooks DJ. Correlating rates of cerebral atrophy in Parkinson's disease with measures of cognitive decline. J Neural Transm 2001;108:571–580.
10. Riekkinen P Jr, Kejonen K, Laakso MP, Soininen H, Partanen K, Riekkinen M. Hippocampal atrophy is related to impaired memory, but not frontal functions in non-demented Parkinson's disease patients. Neuroreport 1998;9:1507–1511.
11. Burton EJ, McKeith IG, Burn DJ, Williams ED, OBrien JT. Cerebral atrophy in Parkinson's disease with and without dementia: a comparison with Alzheimer's disease, dementia with Lewy bodies and controls. Brain 2004;127:791–800.
12. Calne DB, Snow BJ, Lee C. Criteria for diagnosing Parkinson's disease. Ann Neurol 1992;32(suppl):S125–S127.
13. McKeith IG, Galasko D, Kosaka K, et al. Consensus guidelines for the clinical and pathologic diagnosis of dementia with Lewy bodies (DLB):

report of the Consortium on DLB International Workshop. Neurology 1996;47:1113–1124.
14. Collins DL, Neelin P, Peters TM, Evans AC. Automatic 3D intersubject registration of MR volumetric data in standardized Talairach space. J Comput Assist Tomogr 1994;18:192–205.
15. Sled JG, Zijdenbos AP, Evans AC. A nonparametric method for automatic correction of intensity nonuniformity in MRI data. IEEE Trans Med Imag 1998;17:87–97.
16. Cocosco CA, Zijdenbos AP, Evans AC. A fully automatic and robust brain MRI tissue classification method. Med Image Anal 2003;7:513–527.
17. Smith S. Fast robust automated brain extraction. Hum Brain Map 2002;17:143–155.
18. Tohka J, Zijdenbos A, Evans AC. Fast and robust parameter estimation for statistical partial volume models in brain MRI. Neuroimage 2004; 23:84–97.
19. Poline JB, Worsley KJ, Evans AC, Friston KJ. Combining spatial extent and peak intensity to test for activations in functional imaging. Neuroimage 1997;5:83–96.
20. Schulz JB, Skalej M, Wedekind D, et al. Magnetic resonance imaging-based volumetry differentiates idiopathic Parkinson's syndrome from multiple system atrophy and progressive supranuclear palsy. Ann Neurol 1999;45:65–74.
21. Ghaemi M, Hilker R, Rudolf J, Sobesky J, Heiss WD. Differentiating multiple system atrophy from Parkinson's disease: contribution of striatal and midbrain MRI volumetry and multi-tracer PET imaging. J Neurol Neurosurg Psychiatry 2002;73:517–523.
22. Morecraft RJ, Geula C, Mesulam MM. Cytoarchitecture and neural afferents of orbitofrontal cortex in the brain of the monkey. J Comp Neurol 1992;323:341–358.
23. Braak H, Braak E. Pathoanatomy of Parkinson's disease. J Neurol 2000;247(suppl 2):3–10.
24. Harding AJ, Halliday GM. Cortical Lewy body pathology in the diagnosis of dementia. Acta Neuropathol (Berl) 2001;102:355–363.
25. Kövari E, Gold G, Herrmann FR, et al. Lewy body densities in the entorhinal and anterior cingulate cortex predict cognitive deficits in Parkinson's disease. Acta Neuropathol (Berl) 2003;106:83–88.
26. Churchyard A, Lees AJ. The relationship between dementia and direct involvement of the hippocampus and amygdala in Parkinson's disease. Neurology 1997;49:1570–1576.
27. Camicioli R, Moore MM, Kinney A, Corbridge E, Glassberg K, Kaye JA. Parkinson's disease is associated with hippocampal atrophy. Mov Disord 2003;18:784–790.
28. Mattila PM, Rinne JO, Helenius H, Dickson DW, Roytta M. Alpha-synuclein-immunoreactive cortical Lewy bodies are associated with cognitive impairment in Parkinson's disease. Acta Neuropathol (Berl) 2000;100:285–290.
29. Posner MI, Petersen SE, Fox PT, Raichle ME. Localization of cognitive operations in the human brain. Science 1988;240:1627–1631.
30. Duncan J, Owen AM. Common regions of the human frontal lobe recruited by diverse cognitive demands. Trends Neurosci 2000;23:475–483.
31. Taylor AE, Saint-Cyr JA, Lang AE. Frontal lobe dysfunction in Parkinson's disease. The cortical focus of neostriatal outflow. Brain 1986;109: 845–883.
32. Ito K, Nagano-Saito A, Kato T, et al. Striatal and extrastriatal dysfunction in Parkinson's disease with dementia: a 6-[18F]fluoro-L-dopa PET study. Brain 2002;125:1358–1365.
33. de la Monte SM, Wells SE, Hedley-Whyte T, Growdon JH. Neuropathological distinction between Parkinson's dementia and Parkinson's plus Alzheimer's disease. Ann Neurol 1989;26:309–320.
34. Brenneis C, Seppi K, Schocke MF, et al. Voxel-based morphometry detects cortical atrophy in the Parkinson variant of multiple system atrophy. Mov Disord 2003;18:1132–1138.
35. Almeida OP, Burton EJ, McKeith I, Gholkar A, Burn D, O'Brien JT. MRI study of caudate nucleus volume in Parkinson's disease with and without dementia with Lewy bodies and Alzheimer's disease. Dement Geriatr Cogn Disord 2003;16:57–63.
36. Laakso MP, Partanen K, Riekkinen P, et al. Hippocampal volumes in Alzheimer's disease, Parkinson's disease with and without dementia, and in vascular dementia: an MRI study. Neurology 1996;46:678–681.
37. Esposito G, Kirkby BS, Van Horn JD, Ellmore TM, Berman KF. Context-dependent, neural system-specific neurophysiological concomitants of ageing: mapping PET correlates during cognitive activation. Brain 1999;122:963–979.
38. Dagher A, Owen AM, Boecker H, Brooks DJ. The role of the striatum and hippocampus in planning: a PET activation study in Parkinson's disease. Brain 2001;124:1020–1032.
39. Lewis SJ, Dove A, Robbins TW, Barker RA, Owen AM. Cognitive impairments in early Parkinson's disease are accompanied by reductions in activity in frontostriatal neural circuitry. J Neurosci 2003;23:6351–6356.
40. Aguirre GK, Zarahn E, D'Esposito M. An area within human ventral cortex sensitive to "building" stimuli: evidence and implications. Neuron 1998;21:373–383.
41. Bar M, Aminoff E. Cortical analysis of visual context. Neuron 2003;38: 347–358.
42. Della-Maggiore V, Sekuler AB, Grady CL, Bennett PJ, Sekuler R, McIntosh AR. Corticolimbic interactions associated with performance on a short-term memory task are modified by age. J Neurosci 2000;20: 8410–8416.
43. Pillon B, Dubois B, Bonnet AM, et al. Cognitive slowing in Parkinson's disease fails to respond to levodopa treatment: the 15-objects test. Neurology 1989;39:762–768.
44. Costa A, Peppe A, Dell'Agnello G, et al. Dopaminergic modulation of visual-spatial working memory in Parkinson's disease. Dement Geriatr Cogn Disord 2003;15:55–66.

Quantification of Human Nicotinic Acetylcholine Receptors with ^{123}I-5IA SPECT

Marcelo Mamede, MD, PhD[1]; Koichi Ishizu, MD, PhD[1]; Masashi Ueda, MS[2]; Takahiro Mukai, PhD[1]; Yasuhiko Iida, PhD[2]; Hidenao Fukuyama, MD, PhD[3]; Tsuneo Saga, MD, PhD[1]; and Hideo Saji, PhD[2]

[1]*Department of Nuclear Medicine and Diagnostic Imaging, Graduate School of Medicine, Kyoto University, Kyoto, Japan;* [2]*Department of Patho-Functional Bioanalysis, Graduate School of Pharmaceutical Science, Kyoto University, Kyoto, Japan; and* [3]*Brain Function Imaging Division, Human Brain Research Center, Graduate School of Medicine, Kyoto University, Kyoto, Japan.*

Neuronal nicotinic acetylcholine receptors (nAChRs) are widely distributed in the human brain, especially the $\alpha_4\beta_2$ subtype of nAChR. The cholinergic systems have roles in various neurophysiologic functions, such as learning, memory, and cognition, whereas normal aging and neurodegenerative diseases have been associated with changes in nAChRs. Recently, 5-iodo-3-(2(S)-azetidinylmethoxy)pyridine (5IA) has been synthesized as a radioligand for imaging nAChRs with SPECT. ^{123}I-5IA shows higher affinity toward the nAChR $\alpha_4\beta_2$ subtype, enhanced receptor subtype selectivity, good safety, and low nonspecific binding. **Methods:** In this study, a SPECT quantitative study of human nAChRs binding with ^{123}I-5IA was conducted in healthy volunteers. An arterial input function was obtained for each subject and a 2-compartment model was used to determine the kinetic parameters of ^{123}I-5IA using data from a 6-h scan. The distribution volume (V_T) (mL/mL), which is related to the number of unoccupied binding sites in the brain, was calculated and values were compared with results of a graphical analysis (Logan plot, V_{LG}). **Results:** Analysis of the unmetabolized compound showed a high parent fraction of ^{123}I-5IA in plasma. The results from the 2-compartment model analysis showed high V_T values for the thalamus; moderate values for the brain stem, cerebellum, and basal ganglia; and low values for the cortical regions. Good agreement was observed between V_T values and results of autoradiographic experiments done in vitro for nAChR density in human brain. A high correlation index was observed between distribution volumes from model and graphical analyses. **Conclusion:** Our results indicated that ^{123}I-5IA SPECT is suitable for the quantification of nAChRs in human brain.

Key Words: 5-^{123}I-iodo-3-(2(S)-azetidinylmethoxy)pyridine; SPECT; nicotinic acetylcholine receptors; human brain; distribution volume; quantitative measurement; Logan plot; compartmental model analysis

J Nucl Med 2004; 45:1458–1470

Nicotinic acetylcholine receptors (nAChRs) are widely distributed in mammals, appearing in the central and peripheral nervous systems, neuromuscular junctions, and adrenal glands. The majority of high-affinity nAChRs in the brain are of the $\alpha_4\beta_2$ subtype (*1–5*). It has been reported that cholinergic systems play important roles in various neurophysiologic functions such as learning, memory, and cognition (*2,6*). Normal aging and neurodegenerative diseases (such as Alzheimer's disease and Parkinson's disease) have been associated with changes in nAChRs (*2,7–10*). Furthermore, a dose-dependent increase in the subtype in the brain has been observed in chronic nicotine treatment in animal models (*4,11*). This upregulation was also seen in homogenates of autopsied brain samples from smokers (*12,13*), with a return to control levels after cessation of (−)-nicotine treatment (*14*). These findings suggested that upregulation of the $\alpha_4\beta_2$ subtype of nAChR in the brain plays an important role in tobacco tolerance and dependence (*13*).

Therefore, the development of high-affinity radioligands suitable for in vivo imaging of nAChRs, which can provide valuable information from living subjects at different stages of a disease, and the effects of different drugs in patients with neurodegenerative diseases, as well as the upregulation of nAChRs to baseline levels after cessation of treatment with (−)-nicotine or tobacco use, have been of major interest.

Recently, 5-iodo-3-(2(*S*)-azetidinylmethoxy)pyridine (5IA) has been synthesized as a radioligand for imaging nAChRs with SPECT. This compound exhibits extremely high affinity, high selectivity and specificity for the $\alpha_4\beta_2$ subtype of nAChR, relatively low acute toxicity, and acceptable dosimetry (*15–24*).

In this study, a SPECT quantitative study of human nAChRs with ^{123}I-5IA was performed in healthy volunteers. A compartmental model was used to determine the kinetic parameters of ^{123}I-5IA based on the data for a 6-h scan time. Furthermore, due to the necessity of measuring nAChRs in the human brain with a reasonably short scan time for specific achievements, such as in patients with neurodegenerative diseases, a 90-min scan time was also evaluated in another group of healthy subjects.

Received Oct. 30, 2003; revision accepted Mar. 4, 2004.

For correspondence or reprints contact: Koichi Ishizu, MD, PhD, Department of Nuclear Medicine and Diagnostic Imaging, Graduate School of Medicine, Kyoto University, Sakyo, 606-8507, Kyoto, Japan.

E-mail: ishizu@kuhp.kyoto-u.ac.jp

MATERIALS AND METHODS

Groups of Volunteers

The healthy volunteers included in this study were divided into 2 groups. In group 1, 6 young subjects (5 men, 1 woman; age, ~20 y; mean age, 19.5 ± 0.6 y) were included. All subjects underwent a 6-h scan. In group 2, 15 other subjects (6 men, 9 women; age, 20–71 y; mean age, 41.2 ± 18.7 y) were integrated. In this group, a short scan time was applied (90 min). None of the volunteers had a history of either neurologic or psychiatric illness or tobacco use. All subjects gave their written informed consent to participate in this study in compliance with the regulations of the Joint Committee on Clinical Investigation of the Kyoto University Hospital.

Radiolabeling

To a sodium ^{123}I-iodide solution (1,110 MBq) (Nihon Medi-Physics), 100 μg of 5-(tri-*n*-butylstannyl)-3-([1-*t*-butoxycarbonyl-2(*S*)-azetidinyl]methoxy)pyridine, 1.5% acetic acid, 3 mol L HCl, and 5% H_2O_2 solution were added, and the mixture was stirred at 75°C for 15 min. Concentrated HCl was then added and the resulting solution was stirred for another 10 min at 75°C. The mixture was made basic with sodium hydroxide and extracted with ethyl acetate, and the organic layer was evaporated. The residue was purified by reverse-phase high-performance liquid chromatography (HPLC) (Cosmosil 5C18-AR-300, 10 × 250 mm, Nacalai Tesque; 10 mmol L ammonium acetate methanol triethylamine = 752:750:2; 1.5 mL/min; retention time for 5IA = 40 min). After evaporation of the HPLC eluent, the residue was dissolved in 0.9% saline and filtered through a 0.2-μm filter into a sterile vial. Radiochemical purity was >98% and radiochemical yields were ~42%. The specific activity determined from the ultraviolet absorbance at 254 nm was >169 GBq/μmol (the detection limit for this method).

SPECT

All SPECT dynamic scans were acquired with a triple-head rotating γ-camera system (PRISM 3000; Picker International, Inc.) equipped with low-energy, high resolution, fanbeam collimators. This system provides a spatial resolution of 8.0-mm full width at half maximum at the center of the field of view with a sensitivity of 135 cps/MBq. The volunteer's head was placed in a semicylindric head-holder lined with a rubber sponge to prevent motion during the study. Data acquisition was performed in 64 × 64 matrices in a continuous rotation mode with 40 steps for 120° and 1.5 s per step, which translate into 1 min for 1 SPECT dataset. For the first group of subjects, the 6-h scan time, volunteers underwent a 120-min scan (2 min × a 60-frames scan) after intravenous injection of ^{123}I-5IA, followed by 4 sets of 20-min scan (2 min × a 10-frames scan, at 3, 4, 5, and 6 h after the injection), while for the other group of volunteers, only a 90-min (2 min × a 45-frames scan) was performed in each subject.

A cross-calibration between the SPECT scanner and well counter was performed using a series of uniform cylindric phantoms (16-cm inner diameter × 15-cm height) containing an aqueous solution of ^{123}I. The activity on the SPECT images was linearly related to the activity concentration in the phantom measured with the automatic well-type γ-counter (Cobra 2; Packard).

All SPECT images were filtered with a Butterworth filter (cutoff frequency, 0.25; order, 4), and reconstructed using a filtered back-projection algorithm with a ramp filter. Attenuation correction was performed using ellipses outer line approximation and Chang's method (coefficient of 0.06/cm) adjusted for each slice, which assumes that the attenuation process is homogeneous throughout the brain and can be described by an exponential function. The same ellipse size was kept for the different scans of each volunteer. Scatter correction was not applied.

Arterial Input Function

A catheter was inserted into the left brachial artery for blood sampling, while another catheter was inserted into the right cubital vein for the injection of the radioligand. A dose of ~150 MBq ^{123}I-5IA was administered intravenously over a period of 1 min at a constant rate with an infusion pump. The scan started simultaneously with the injection.

An arterial input function was obtained for each volunteer. Twenty-five arterial blood samples were drawn, initially every 10 s during the first 2 min, followed by 15 s during the next minute, and then subsequently at 5, 7, 10, 20, 30, 45, 60, 90, and 120 min (for those subjects with a short scan time, the last sample was not drawn). Additionally, 6 venous blood samples were obtained at 1.5, 2, 3, 4, 5, and 6 h after injection using different vessels. Blood samples were centrifuged at 1,750*g* for 3 min at 4°C. From each sample, 100 μL of plasma were removed and the radioactivity was measured in an automatic well-type γ-counter (Cobra 2; Packard). All radioactivity measurements were decay corrected to the time of radioligand administration. The first 2 venous samples were drawn to verify the suitability of venous blood sampling to be used for the input function instead of arterial sampling. We previously confirmed its suitability in preliminary analytic studies of arterial and venous samples at several time points, including 1.5, 2, 4, and 6 h after injection.

Sixteen samples (1, 2, 3, 5, 7, 10, 20, 30, 45, 60, 90, 120, 180, 240, 300, and 360 min) were analyzed for metabolite determination. An aliquot of 300 μL of plasma was mixed with an equal volume of acetonitrile, and the denatured proteins were removed from the plasma by centrifugation at 1,750*g* for 5 min at 4°C. The radioactivity in the supernatant was analyzed by thin-layer chromatography (TLC) (R_f = 0.55 for ^{123}I-5IA) (LK6DF Silica Gel 60 Å; Whatman). The TLC plates were developed in a solution of 10% ammonium acetate and methanol (1:1). Furthermore, some of the plasma supernatant samples (1, 3, 10, 30, 60, and 120 min) were also analyzed by reverse-phase HPLC (Cosmosil 5C18-AR-300, 4.6 × 150 mm; Nacalai Tesque) at a flow rate of 1.0 mL/min (retention time for ^{123}I-5IA = 10 min).

The unmetabolized fraction, M(t), of the arterial input function was determined from the ratio of parent compound counts to the total plasma counts derived from TLC results. The following empiric equation was used to describe α and β:

$$M(t):1\ [1 + (\alpha t)^2]^{\beta}, \qquad \text{Eq. 1}$$

where the parameters α and β were estimated by nonlinear least-squares fitting. This empiric equation was designed to equal 1 at time 0 with a zero first derivative. Metabolite correction was performed by plotting the activity in arterial plasma samples against the time.

Data Analysis

Initially, 60 circular regions of interest (ROIs) (21 pixels per circle) were manually drawn on a 120-min composite transaxial SPECT image of each subject. The ROIs were distributed among various regions (basal ganglia, thalamus, brain stem, cerebellum, and frontal, parietal, temporal, and occipital cortices) on both sides. Then, ROIs were placed on the delayed scans (3-, 4-, 5-, and

6-h scans). To accomplish the best coregistration between the initial scan (120 min) and subsequent delayed scans (4 sets of 20 min), the slice with the highest tissue count (thalamus region) was identified for each scan. Then, based on that slice, the exact position of the ROIs used on the 120-min scan were repositioned on the other scans using an image analysis package (Dr. View; Asahi-Kasei) and dedicated software. Thus, we could maintain the same ROI position for the same region in different image sets. For the 90-min scan time, the same procedure was used. However, no coregistration with another scan time was necessary. ROI data were further decay corrected. SPECT data were calibrated to the well counter used to measure the injected activity. Time–activity curves were generated for each ROI using the same image analysis package (Dr. View).

Derivation of Receptor Parameters

The analysis of ^{123}I-5IA distribution begins with the kinetic model depicted in Figure 1A. Owing to the limited statistical quality of SPECT data, we initially proposed a model that has only 2 tissue compartments. The model consists of 1 blood compartment, representing the arterial plasma concentration of unchanged tracer (C_p), a tissue compartment (C_{f+ns}) that encloses free ligand in tissue (C_f) plus ligand bound to nonspecific sites (C_{ns}), and another tissue compartment representing ligand bound to specific sites (C_s). In this model, the free and nonspecifically bound tissue compartments are assumed to equilibrate rapidly. The units of concentration (or radioactivities) for each compartment presented in this article are in kBq g.

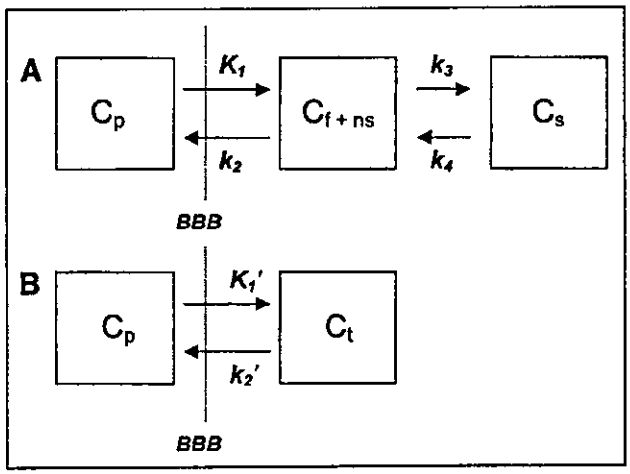

FIGURE 1. (A) Three-compartment, 4-parameter kinetic model. This model consists of 1 blood compartment (C_p), a tissue compartment (C_{f+ns}) that encloses the free ligand in tissue (C_f) plus ligand bound to nonspecific sites (C_{ns}), and another tissue compartment representing ligand bound to specific sites (C_s). Free and nonspecifically bound tissue compartments are assumed to equilibrate rapidly. Rate parameters (K_1, k_2, k_3, and k_4) describe exchange across blood–brain barrier (*BBB*), association and dissociation from sites in free plus nonspecifically bound compartment, and association and dissociation from sites in specifically bound compartment. (B) Two-compartment, 2-parameter kinetic model. This configuration simplifies the model described in A by combining free plus nonspecifically bound compartment and specific compartment into a single compartment (C_{f+ns+s}) and assumes that rate constants k_3 and k_4 are rapid compared with *BBB* transport rates.

The equilibrium distribution volume of a compartment i (V_i; mL g) was defined as the equilibrium ratio of the tracer concentration in this compartment (C_i) to the free arterial concentration ($C_p f_1$, where f_1 represents the fraction of unbound to plasma proteins unmetabolized parent radioligand activity in plasma):

$$V_i = C_i / C_p f_1. \quad \text{Eq. 2}$$

V_{f+ns} and V_s are the equilibrium distribution volumes of the free plus nonspecific compartments and specific compartment, respectively. V_{f+ns+s} (V_T) is the total regional equilibrium distribution volume, equal to the sum of V_{f+ns} and V_s.

The tracer concentration over time in C_{f+ns} and C_s is given by:

$$dC_{f+ns}(t)/dt = K_1 C_p(t) - k_2 C_{f+ns}(t) - k_3 C_{f+ns}(t) + k_4 C_s(t). \quad \text{Eq. 3}$$

$$dC_s(t)/dt = k_3 C_{f+ns}(t) - k_4 C_s(t). \quad \text{Eq. 4}$$

The parameters are defined as follows:

$$K_1 = FE_0 = f(1 - e^{-PS/F}) \text{ (mL g min)}. \quad \text{Eq. 5}$$

$$k_2 = K_1 / V_{f+ns} f_1 \text{ (min}^{-1}\text{)}. \quad \text{Eq. 6}$$

$$k_3 = k_{on} B_{max}' / V_{f+ns} \text{ (min}^{-1}\text{)}. \quad \text{Eq. 7}$$

$$k_4 = k_{off} \text{ (min}^{-1}\text{)}. \quad \text{Eq. 8}$$

$$K_d = k_{off} / k_{on}. \quad \text{Eq. 9}$$

$$k_3 / k_4 = B_{max}' / K_d = BP. \quad \text{Eq. 10}$$

The rate parameter K_1 represents the delivery rate constant from plasma to compartment C_{f+ns}, and k_2 defines the rate constant of return from compartment C_{f+ns} to plasma. We assume that, at equilibrium, the concentration of free tracer in tissue water equals the concentration in plasma water. The parameter k_3 is the rate constant of transfer from compartment C_{f+ns} to C_s, and the parameter k_4 is equal to k_{off}, the dissociation rate from the receptor.

The parameter F is regional blood flow (mL g min). E_0 is the single-pass extraction fraction of ligand into brain. PS is the permeability-surface area product (mL g min). k_{on} is the biomolecular association rate between ligand and receptor (g pmol min). B_{max}' is the receptor density or concentration of "unoccupied" receptors (pmol g). k_{off} is the dissociation rate of ligand from the receptor complex (min^{-1}), and K_d is the equilibrium ligand binding constant for the specific receptor site (pmol g). The ratio of receptor-related parameters B_{max}' and K_d has been previously referred to as the binding potential (BP) (*25*). The solution to this model form is given by:

$$C_t(t) = K_1 (x_2 - x_1)[(k_3 + k_4 - x_1)e^{-x_1 t} + (x_2 - k_3 - k_4)e^{-x_2 t}] \otimes C_p(t), \quad \text{Eq. 11}$$

where $C_t(t)$ is defined as concentration in tissue ($C_{f+ns} + C_s$):

$$x_{1,2} = \frac{(k_2 + k_3 + k_4) \pm \sqrt{(k_2 + k_3 + k_4)^2 - 4k_2k_4}}{2}. \quad \text{Eq. 12}$$

$\otimes$ represents the mathematic operation of convolution.

If the binding and dissociation of ligand from the specific receptor compartment are rapid compared with the transport parameters K_1 and k_2, the model can be further reduced to a single tissue compartment that contains free, nonspecifically bound, and specifically bound ligand, as shown in Figure 1B. The kinetic parameters of this simplified model are described as follows:

$$K_1' = FE_0 = f(1 - e^{-PSF}). \quad \text{Eq. 13}$$

$$k_2' = k_2\,1 + k_3\,k_4 = K_1\,V_{f+ns}'f_1 = K_1\,V_{f+ns+s}f_1. \quad \text{Eq. 14}$$

$$V_{f+ns}' = V_{f+ns+s} = K_1\,k_2' = V_T. \quad \text{Eq. 15}$$

The solution equation to this model form is given by:

$$C_t(t) = K_1 \cdot e^{-k_2't} \otimes C_p(t). \quad \text{Eq. 16}$$

Since k_3 and B_{max}' are no longer isolated model parameters, receptor information in this model configuration is represented only by V_T. As the ratio of the association to dissociation rate ($k_3\,k_4$) becomes progressively higher, the specific distribution volume term dominates and V_{f+ns}' yields a progressively better estimate of B_{max}'.

Due to its simplicity and independence from a model—that is, no knowledge is required of the compartmental configuration of the underlying data—a graphical method of analysis (*26*) was also used. In SPECT, regions of brain tissue are sampled by drawing a ROI. The radioactivities in a ROI at time t can be expressed as:

$$ROI(t) = C_t(t) + VC_p(t). \quad \text{Eq. 17}$$

that is, the sum of radioactivities from all compartments in a given ROI plus the contribution from regional blood volume V. V is estimated at 5% and often has a negligible contribution after the initial part of the study. Thus, Equation 17 can be rearranged into Equations 18 and 19 for the 3- and 2-compartmental models, respectively:

$$\int_0^t \mathrm{ROI}(t')dt'\ \mathrm{ROI}(t) =$$

$$[K_1\,k_2(1 + k_3\,k_4) + V]\int_0^t C_p(t')dt'\ \mathrm{ROI}(t) + int. \quad \text{Eq. 18}$$

$$\int_0^t \mathrm{ROI}(t')dt'\ \mathrm{ROI}(t) = (K_1\,k_2' + V)\int_0^t C_p(t')dt'\ \mathrm{ROI}(t) + int.$$

Eq. 19

Equations 18 and 19 are linear forms when the last term (*int*) is constant. The points plotted are defined by the scanning time t.

Plotting $\int_0^t \mathrm{ROI}(t')dt'\ \mathrm{ROI}(t)$ versus $\int_0^t C_p(t')dt'\ \mathrm{ROI}(t)$ for time t, a representative plot of a ROI is linear after some time t^*. The slope of this linear function represents the total distribution volume plus the blood contribution, here defined as V_{LG}. In this study, the K_1 value from the Logan plot is designated as K^*_1 as well as k^*_2. The effects of blood flow and capillary permeability are implicitly included in K^*_1 and k^*_2. For the 2-compartment model, nonspecific binding is also included in k^*_2. Estimates of K^*_1 can be calculated by taking the ratio of the slope (V_{LG} value, neglecting V) of the linear function, while k^*_2 can be calculated by taking the ratio of K^*_1 to V_{LG}. This will be valid for the 2-compartment model when the second term, the intercept, is small compared with the first.

Statistical Analysis

All data are expressed as the mean ± SD and the percentage of the rate constants (coefficient of variation [%COV]) (100 × SD/mean). The distribution volumes obtained from the different regions in the brain were analyzed using 1-way ANOVA with the Bonferroni protected least-significant difference test. A factorial ANOVA was also performed considering interacted factors, different time intervals (90 and 360 min) and regions in the brain, to determine the V_T values. An analysis of correlation (Pearson test) between distribution volumes calculated from different methods of analyses was performed. A Student t test was also applied for comparisons between the first (90-min scan time) and second group of volunteers with matched age for the same region. All tests were 2-sided, and P values <0.05 were considered significant.

RESULTS

Plasma Analysis

For group 1 volunteers and the 6-h scan time, the peak plasma activity occurred between 70 and 80 s after injection in all subjects and decreased rapidly to 3.6%–7.9% of the peak level in 10 min. Analysis of the unmetabolized compound by TLC demonstrated a high parent fraction of ^{123}I-5IA in the plasma (89.9% ± 5.1%) in the first minute. These values were estimated using Equation 1, which showed good fitting for all volunteers. ^{123}I-5IA was rapidly metabolized and the unchanged fraction represented 46.6% ± 9.5% and 27.4% ± 6.0% of total plasma activity at 20 and 60 min, respectively. Figure 2 shows typical radioactivity in whole plasma and the free parent compound of ^{123}I-5IA throughout the scan time. For the 90-min scan time, the second group of volunteers, the results were similar to those described for the 6-h scan time.

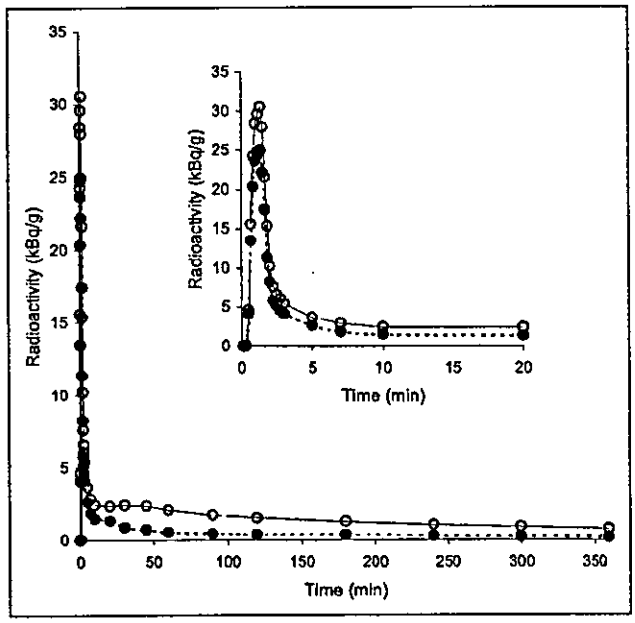

FIGURE 2. Typical plasma time–activity curves show radioactivity in whole plasma (○) and free parent (●) compound of ^{123}I-5IA acquired throughout scan time (360 min) after intravenous bolus injection of 172 MBq ^{123}I-5IA in 20-y-old man (subject 4). Inset shows same plasma time–activity curves for short period (20 min). Peak plasma activity occurred at 80 s after injection of ^{123}I-5IA and decreased rapidly to 5.9% of peak level in 10 min.

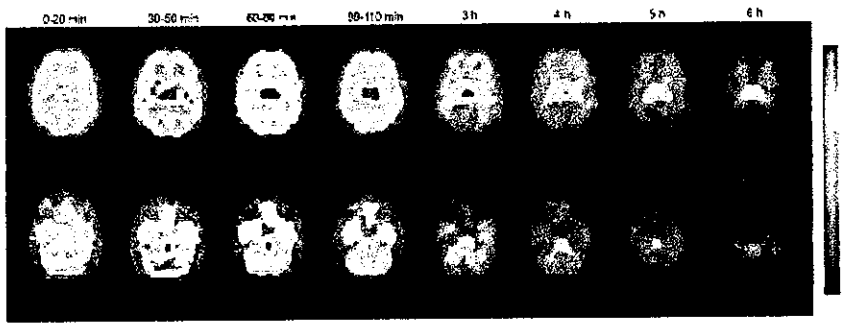

FIGURE 3. Selected slices of human brain after intravenous bolus injection of 172 MBq ^{123}I-5IA in 20-y-old man (subject 4). Reconstructed tranverse slices were summed according to scan time (0–20 min, 30–50 min, 60–80 min, 90–110 min, 3 h, 4 h, 5 h, and 6 h). Top row of slices represents midpart of brain (frontal, temporal, occipital, thalamus, and basal ganglia). Bottom row represents slices from inferior part of human brain (cerebellum, brain stem, and temporal cortex). ^{123}I-5IA SPECT images clearly show cortical regions, cerebellum, thalamus, brain stem, and basal ganglia. Thalamus and brain stem exhibited higher uptake than other structures in brain, which became more prominent throughout scan time.

The suitability of using venous blood sampling for the input function was confirmed by the good agreement of the radioactivity in whole plasma (0.00099 ± 0.00015 [arterial] and 0.00100 ± 0.00013 [venous] %dose/mL at 90 min; 0.00090 ± 0.00011 [arterial] and 0.00094 ± 0.00012 [venous] %dose/mL at 120 min) and the ratio of measured free parent fraction between arterial and venous blood samples drawn at 90 and 120 min (0.29 ± 0.05 [arterial] and 0.27 ± 0.04 [venous] at 90 min; 0.20 ± 0.04 [arterial] and 0.20 ± 0.04 [venous] at 120 min). Thus, venous blood sampling is a simple and acceptable choice for input function following 2 h after injection of 5IA.

The results obtained by TLC were in agreement with those from HPLC at 1, 3, 10, 30, 60, and 120 min after injection. The labeled metabolites were not identified, but they were more polar than the parent compound and may not cross the blood–brain barrier.

Brain Imaging Analysis

For all volunteers (first and second groups), ^{123}I-5IA-SPECT images clearly revealed the cortical regions, cerebellum, thalamus, brain stem, and basal ganglia. Initially, within the first 20 min, the images seemed to have a similar pattern as cerebral blood flow. Subsequently, the thalamus and brain stem showed higher uptake than the other structures in the brain, which became more prominent throughout the scan time. Figure 3 shows a typical 6-h scan time distribution and the dynamics of ^{123}I-5IA in the brain throughout the scan time. No side effects were observed during the scan in any volunteers.

Figure 4 shows typical 6-h scan time–activity curves of ^{123}I-5IA in the thalamus, brain stem, and frontal cortex. The concentration of radioactivity was highest in the thalamus followed by the brain stem. An intermediate accumulation of radioactivity of ^{123}I-5IA was observed in the cerebellum, basal ganglia, and cortical regions. In all subscripts, the peaks of radioactivity in the thalamus and brain stem occurred at 90–110 min and 70–90 min after injection of ^{123}I-5IA, respectively. These peaks were observed later than in the other brain regions, which were found at around 30–50 min. A differential dissociation of ^{123}I-5IA from the binding sites was noted in the brain. The cortical regions, basal ganglia, and cerebellum showed an earlier dissociation than the brain stem and thalamus. These findings reflected a distinct regional distribution of nAChRs in the human brain (*27,28*).

For the second group of volunteers, the pattern of radioactivity in the brain was almost the same as that described for the first group, except for the thalamus. The peak of radioactivity in the thalamus could not be seen precisely throughout the scan time. The time–activity curve in the cortical regions, basal ganglia, and cerebellum had a similar pattern observed during the 6-h scan time.

Based on these data, a quantitative analysis of nAChR density was performed. First, the 3-compartment model analysis was performed. The 4-parameter model configura-

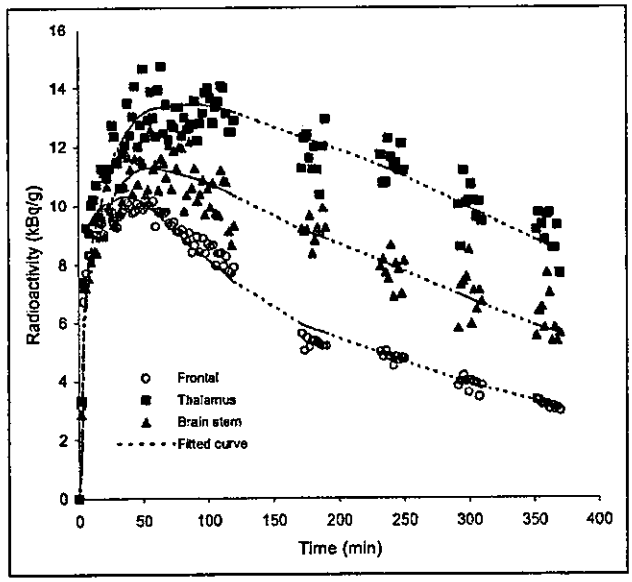

FIGURE 4. Typical time–activity curves of ^{123}I-5IA in regions of human brain after intravenous injection of 172 MBq ^{123}I-5IA in 20-y-old man (subject 4). Concentration of radioactivity in brain was highest in thalamus followed by brain stem. Little accumulation of radioactivity was observed in cortical regions (represented by frontal cortex).

TABLE 1

^{123}I-5IA Parameter Estimates for 2-Compartment, 2-Parameter Model Analysis Using 6-Hour Scan Time (6 Healthy Volunteers)

	Frontal cortex			Parietal cortex			Temporal cortex			Occipital cortex			Basal ganglia			Thalamus			Brain stem			Cerebellum		
Volunteer	V_T	K_1'	k_2'	V_T	K_1'	k_2'	V_T	K_1'	k_2'	V_T	K_1'	k_2'	V_T	K_1'	k_2'	V_T	K_1'	k_2'	V_T	K_1'	k_2'	V_T	K_1'	k_2'
1																								
Mean	19.0	0.21	0.011	17.8	0.22	0.012	18.5	0.20	0.011	17.5	0.20	0.012	23.1	0.20	0.009	47.1	0.22	0.005	35.2	0.21	0.006	19.9	0.23	0.012
SD	0.2	0.01	0.001	0.2	0.01	0.000	0.7	0.01	0.001	0.7	0.01	0.001	0.4	0.02	0.001	1.8	0.01	0.000	1.2	0.01	0.000	0.9	0.02	0.001
%COV	1.1	6.0	5.4	1.1	2.8	3.5	3.5	5.4	6.6	4.1	3.7	6.6	1.7	7.9	8.7	3.7	3.2	5.3	3.5	6.6	4.9	4.6	6.7	9.1
2																								
Mean	13.6	0.21	0.016	13.4	0.22	0.016	13.1	0.20	0.016	12.0	0.21	0.018	15.3	0.21	0.014	31.3	0.19	0.006	22.6	0.19	0.009	17.0	0.19	0.011
SD	0.3	0.01	0.000	0.4	0.01	0.001	0.6	0.01	0.001	0.5	0.01	0.001	0.7	0.01	0.001	1.9	0.01	0.000	0.9	0.00	0.000	0.1	0.01	0.000
%COV	2.0	2.4	2.1	3.1	3.5	6.2	4.9	5.5	6.7	3.8	5.1	6.4	4.4	5.2	5.9	6.2	2.9	5.7	3.8	1.3	4.4	0.9	3.4	3.6
3																								
Mean	16.2	0.27	0.017	16.3	0.26	0.016	16.6	0.26	0.016	15.2	0.27	0.018	21.3	0.23	0.011	37.1	0.23	0.006	26.3	0.24	0.009	20.1	0.28	0.014
SD	0.3	0.01	0.001	0.5	0.02	0.001	0.3	0.01	0.001	0.5	0.01	0.001	0.6	0.00	0.000	1.8	0.02	0.001	1.3	0.01	0.001	0.5	0.01	0.001
%COV	2.2	3.6	4.1	2.8	6.9	7.0	1.6	3.9	4.3	3.6	4.8	6.5	2.7	1.2	3.1	4.7	7.2	9.5	5.0	3.6	8.4	2.4	4.9	5.0
4																								
Mean	12.9	0.19	0.015	12.6	0.18	0.015	12.7	0.18	0.014	11.6	0.20	0.017	15.0	0.17	0.011	29.1	0.18	0.006	20.0	0.17	0.009	15.8	0.19	0.012
SD	0.6	0.01	0.001	0.3	0.00	0.000	0.5	0.01	0.001	0.3	0.01	0.001	0.4	0.02	0.002	1.8	0.01	0.001	1.3	0.01	0.001	0.5	0.01	0.000
%COV	4.3	8.2	5.2	2.1	2.0	3.4	3.9	6.5	4.4	2.9	3.7	4.4	2.4	13.2	15.2	6.1	6.8	9.0	6.6	6.8	8.9	3.0	4.0	3.4
5																								
Mean	13.0	0.24	0.019	11.9	0.23	0.019	12.6	0.23	0.018	11.3	0.25	0.023	14.4	0.23	0.016	29.0	0.23	0.008	20.0	0.21	0.010	15.6	0.23	0.015
SD	0.5	0.01	0.001	0.5	0.02	0.002	0.2	0.01	0.001	0.4	0.01	0.001	0.4	0.01	0.001	1.5	0.01	0.000	1.1	0.01	0.001	0.7	0.01	0.001
%COV	4.1	5.7	3.6	4.5	7.9	8.5	1.7	4.8	3.5	3.4	3.2	5.1	3.0	3.3	5.1	5.1	3.4	4.6	5.4	4.0	8.1	4.3	2.7	4.2
6																								
Mean	13.1	0.18	0.014	13.3	0.19	0.014	13.9	0.17	0.012	11.6	0.18	0.016	16.3	0.17	0.010	32.4	0.18	0.006	24.2	0.17	0.007	18.4	0.21	0.012
SD	0.6	0.01	0.001	0.6	0.01	0.001	0.1	0.01	0.000	0.1	0.01	0.001	0.1	0.01	0.001	1.2	0.01	0.001	0.8	0.00	0.000	0.9	0.01	0.001
%COV	4.4	6.8	4.0	4.5	4.9	8.3	1.1	3.1	2.6	1.2	5.3	4.9	0.8	5.0	5.3	3.7	8.1	9.3	3.3	2.3	1.8	4.9	6.0	9.1
All																								
Mean	14.6	0.22	0.015	14.2	0.21	0.015	14.6	0.21	0.014	13.2	0.22	0.017	17.6	0.20	0.012	34.3	0.21	0.006	24.7	0.20	0.008	17.8	0.22	0.013
SD	2.5	0.03	0.003	2.3	0.03	0.002	2.4	0.03	0.003	2.6	0.03	0.004	3.7	0.03	0.003	6.9	0.03	0.001	5.7	0.02	0.002	2.0	0.03	0.001
%COV	16.8	15.1	16.8	16.3	12.5	14.8	16.7	16.8	18.8	19.4	15.0	20.6	20.9	13.3	21.2	20.2	12.5	17.4	22.9	12.3	18.7	11.0	14.9	11.8

Values for V_T are given in mL/g, for K_1' in mL/g/min, and for k_2' in min^{-1}.

tion could not appropriately fit the present data and inadequately identified the rate parameter constants. Variable lower V_T values in different regions in the human brain were also observed (data not shown). The 3-compartment model could not provide goodness of fit, indicating that the association and dissociation of ligand from the specific receptor compartment were rapid, and the nonspecific and specific compartments mixed instantaneously. Thus, all analyses were made with the 2-compartment model.

Table 1 summarizes the V_T, K_1', and k_2' values from 2-compartment model analysis in different brain regions for each subject studied in the first group. The highest V_T values were found in the thalamus (ANOVA, $P < 0.01$). Subsequently, the brain stem, cerebellum, and basal ganglia were assembled in a group of moderate $\alpha_4\beta_2$ binding density. No statistically significant difference was observed between them. The V_T values of the brain stem and cerebellum were higher ($P < 0.05$) than the values for the cortical regions (frontal, parietal, temporal, and occipital cortices), whereas for the basal ganglia this finding was observed only for the occipital cortex ($P < 0.05$). The remaining regions were arranged in a group of low-binding density. The relative performance of the 2-parameter model configuration can be evaluated through comparison of the estimated parameters using %COV. The estimation of parameters V_T, K_1', and k_2' is relatively stable and the variation was small in each subject across all brain regions (Table 1). The intersubject variability was also reasonable and generally ranged from 11% to 21%.

Figure 5 illustrates a typical example of graphical analysis applied to ROIs from the frontal cortex, thalamus, and brain stem. The linear region begins at about 4 min after injection (t^*). The same time point (t^*) was observed for all subjects across all regions. The slope is greatest for the ROI from the thalamus, followed by the brain stem and frontal cortex. Table 2 lists V_{LG}, K^*_1, and k^*_2 determined by the graphical analysis in the brain. The pattern of distribution of V_{LG} in the human brain was the same as that of V_T in all subjects at the 6-h scan time, as was the variability accounted for by %COV.

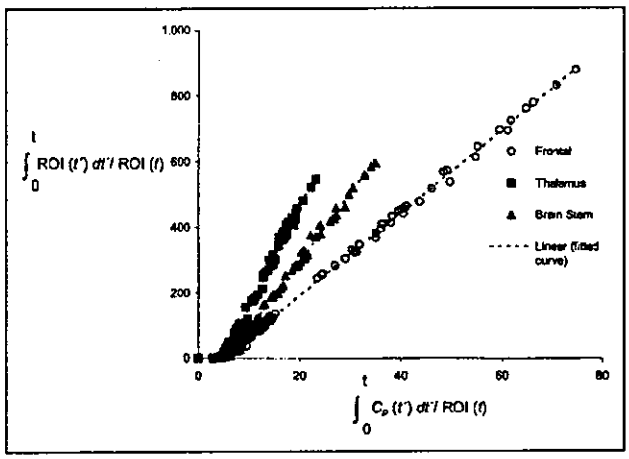

FIGURE 5. Typical example of graphical analysis applied to ROIs from frontal cortex, thalamus, and brain stem (subject 4). At about 4 min after injection (t^*), a representative plot of ROI is linear. Slope of this linear function represents total distribution volume plus blood contribution (V_{LG}). Greatest slope is for ROI from thalamus, followed by brain stem and frontal cortex. Slopes representative of linear curves are 10.5, 15.7, and 13.3, respectively.

Parameter estimates as a function of the duration of data used in the fits from the 6-h scan time are shown in Table 3. Estimations were made using a short time interval (0–90 min) for the entire 360-min sequence. The estimation of parameters V_T, K_1', and k_2' is quite stable in the cortical regions and basal ganglia throughout the time intervals. On the other hand, some variability was observed in the thalamus, brain stem, and cerebellum for a shorter scan time. One-way ANOVA demonstrated no significant difference between those time intervals across all regions.

Table 4 summarizes the receptor parameter values (V_T, K_1', and k_2') from the 2-compartment model analysis in different brain regions for each volunteer in a short scan time (90 min). Results of the first 6 volunteers (subjects 1–6, group 1) were generated from a 6-h scan time when a short time interval (0–90 min) was applied. Results of the remaining 15 volunteers (subjects 7–21, group 2) were calculated from a single 90-min scan time. To verify the homogeneity of V_T values determined between these 2 groups of subjects, aged-matching comparisons were done. The V_T values from the first group of subjects were compared with those from the second group with the same age. No statistical differences were observed between V_T values for all regions in the brain between these 2 groups of subjects for the same age. The distribution of V_T values for all subjects with a short scan time (first and second groups) had a pattern similar to that observed for a 6-h scan time. The thalamus showed also the highest V_T value (ANOVA, $P < 0.01$).

DISCUSSION

To our knowledge, this article describes the first quantitative study of ^{123}I-5IA SPECT for the measurement of nAChRs in the human brain. There were several reasons for selecting ^{123}I-5IA to quantitatively study nAChRs in the human brain. First, there were several previous studies of radioiodine-labeled compounds of these series with extremely high affinity and selectivity for the nAChR $\alpha_4\beta_2$ subtype in vivo, with low nonspecific binding, good persistence in animal and human brain, and acceptable dosimetry for human use (*19–24*). Second, the procedure for the synthesis of ^{123}I-5IA is not complicated, the radiochemical purity is high (>98%), the radiochemical yields are good (42%), and highly specific radioactivity can be achieved with this radiolabeling sequence (*18*). Third, the longer imaging time frame afforded with ^{123}I (half-life = 13.2 h) and the prevalence of SPECT scanners in laboratories

TABLE 2

^{123}I-5IA Parameter Estimates for Graphical Analysis from 2-Compartment Model Using 6-Hour Scan Time (6 Healthy Volunteers)

	Frontal cortex			Parietal cortex			Temporal cortex			Occipital cortex			Basal ganglia			Thalamus			Brain stem			Cerebellum		
Volunteer	V_{LG}	K^*_1	k^*_2	V_{LG}	K^*_1	k^*_2	V_{LG}	K^*_1	k^*_2	V_{LG}	K^*_1	k^*_2	V_{LG}	K^*_1	k^*_2	V_{LG}	K^*_1	k^*_2	V_{LG}	K^*_1	k^*_2	V_{LG}	K^*_1	k^*_2
1																								
Mean	18.4	0.22	0.012	17.6	0.23	0.013	18.2	0.20	0.011	17.9	0.20	0.011	23.1	0.20	0.009	45.6	0.23	0.005	34.8	0.21	0.006	20.3	0.23	0.012
SD	0.4	0.02	0.001	0.5	0.01	0.001	1.1	0.01	0.001	0.4	0.00	0.000	0.4	0.02	0.001	1.4	0.01	0.000	1.5	0.01	0.000	0.9	0.02	0.002
%COV	2.0	7.0	6.5	2.7	5.0	7.5	6.2	6.9	10.7	2.5	2.0	3.4	1.6	8.3	9.1	3.0	3.1	5.4	4.3	6.0	2.7	4.3	9.5	13.2
2																								
Mean	13.2	0.23	0.017	13.1	0.22	0.017	13.0	0.21	0.016	12.0	0.22	0.018	15.5	0.21	0.014	31.6	0.19	0.006	23.0	0.19	0.008	17.2	0.19	0.011
SD	0.4	0.01	0.001	0.5	0.01	0.002	0.8	0.01	0.001	0.5	0.02	0.002	1.0	0.01	0.001	1.1	0.01	0.000	1.1	0.00	0.000	0.3	0.01	0.001
%COV	3.2	5.5	6.9	4.0	6.1	10.1	5.9	5.5	6.5	4.5	7.8	10.9	6.5	5.4	9.6	3.3	3.5	3.8	4.7	1.0	5.1	1.9	4.0	5.6
3																								
Mean	16.1	0.27	0.017	16.6	0.27	0.016	16.9	.026	0.016	15.5	0.28	0.018	21.9	0.23	0.011	37.3	0.24	0.006	26.8	0.24	0.009	20.9	0.27	0.013
SD	0.5	0.02	0.002	0.6	0.03	0.002	0.6	0.01	0.001	0.6	0.02	0.001	1.1	0.01	0.001	1.4	0.01	0.000	1.2	0.01	0.001	0.5	0.02	0.001
%COV	3.2	7.5	9.6	3.6	10.1	11.3	3.5	4.3	6.9	4.0	6.2	7.1	4.8	2.4	7.1	3.7	5.7	6.1	4.6	4.0	8.5	2.2	5.6	6.5
4																								
Mean	12.6	0.20	0.016	12.2	0.20	0.017	12.4	0.19	0.015	11.2	0.23	0.021	14.9	0.17	0.012	28.9	0.19	0.007	19.5	0.18	0.009	16.1	0.20	0.012
SD	0.3	0.02	0.001	0.04	0.01	0.001	0.4	0.02	0.001	0.4	0.02	0.003	0.5	0.02	0.002	2.0	0.01	0.001	1.1	0.01	0.001	0.4	0.01	0.001
%COV	2.5	9.4	9.2	3.2	4.0	6.2	3.3	8.9	8.8	3.6	9.5	12.3	3.3	12.8	15.2	7.0	3.8	9.0	5.5	7.2	7.6	2.7	5.0	5.1
5																								
Mean	12.9	0.27	0.021	11.8	0.24	0.021	12.6	0.24	0.019	11.4	0.26	0.023	15.2	0.22	0.014	29.0	0.24	0.008	20.3	0.22	0.011	16.1	0.23	0.015
SD	0.3	0.02	0.002	0.4	0.02	0.001	0.3	0.01	0.001	0.5	0.02	0.003	0.5	0.01	0.001	1.0	0.01	0.000	0.9	0.01	0.001	0.6	0.01	0.001
%COV	2.4	7.3	7.3	3.5	6.2	5.8	2.3	5.7	4.5	4.2	7.9	11.4	3.1	3.4	5.7	3.3	3.0	5.6	4.4	3.3	6.3	3.7	3.4	3.8
6																								
Mean	12.5	0.21	0.017	13.0	0.21	0.016	13.3	0.19	0.014	11.7	0.20	0.017	16.0	0.18	0.011	31.5	0.19	0.006	22.3	0.19	0.008	18.2	0.22	0.012
SD	0.5	0.01	0.001	0.4	0.02	0.002	0.2	0.01	0.001	0.3	0.02	0.002	0.4	0.01	0.001	1.5	0.01	0.000	0.6	0.01	0.000	0.8	0.01	0.001
%COV	4.0	7.1	5.3	2.7	8.7	9.7	1.2	5.4	6.1	2.4	8.8	10.4	2.7	5.8	7.3	4.8	5.4	3.6	2.8	3.0	1.9	4.5	5.6	8.6
All																								
Mean	14.3	0.23	0.017	14.0	0.23	0.017	14.4	0.22	0.015	13.3	0.23	0.018	17.8	0.20	0.012	34.0	0.21	0.006	24.5	0.20	0.009	18.1	0.23	0.013
SD	2.4	0.03	0.003	2.4	0.02	0.002	2.5	0.03	0.003	2.8	0.03	0.004	3.7	0.02	0.002	6.4	0.03	0.001	5.7	0.02	0.001	2.1	0.03	0.001
%COV	16.9	13.2	16.5	17.4	10.5	14.9	17.4	13.7	17.0	20.8	14.7	22.1	20.9	11.4	17.9	19.0	12.1	17.2	23.2	11.3	17.1	11.4	12.2	9.3

Values for V_{LG} are given in mL/g, for K^*_1 in mL/g/min, and for k^*_2 in min^{-1}.

TABLE 3

^{123}I-5IA Parameter Estimates For 2-Compartment, 2-Parameter Model Analysis with 6-Hour Scan Time at Different Time Intervals

	Frontal cortex			Parietal cortex			Temporal cortex			Occipital cortex			Basal ganglia			Thalamus			Brain stem			Cerebellum		
Volunteer	V_T	K_1'	k_2'	V_T	K_1'	k_2'	V_T	K_1'	k_2'	V_T	K_1'	k_2'	V_T	K_1'	k_2'	V_T	K_1'	k_2'	V_T	K_1'	k_2'	V_T	K_1'	k_2'
360 min																								
Mean	14.6	0.22	0.015	14.2	0.21	0.015	14.6	0.21	0.014	13.2	0.22	0.017	17.6	0.20	0.012	34.3	0.21	0.006	24.7	0.20	0.008	17.8	0.22	0.013
SD	2.5	0.03	0.003	2.3	0.03	0.002	2.4	0.03	0.003	2.6	0.03	0.004	3.7	0.03	0.003	6.9	0.03	0.001	5.7	0.02	0.002	2.0	0.03	0.001
%COV	16.8	15.1	16.8	16.3	12.5	14.8	16.7	16.8	18.8	19.4	15.0	20.6	20.9	13.3	21.2	20.2	12.5	17.4	22.9	12.3	18.7	11.0	14.0	11.8
90 min																								
Mean	14.8	0.21	0.015	14.1	0.22	0.016	14.1	0.21	0.015	12.6	0.23	0.018	16.2	0.22	0.014	28.4	0.23	0.009	21.8	0.21	0.010	16.1	0.24	0.015
SD	2.1	0.03	0.002	2.5	0.03	0.003	1.9	0.04	0.003	2.1	0.03	0.004	3.8	0.04	0.004	7.2	0.04	0.003	4.8	0.03	0.003	2.1	0.04	0.003
%COV	14.3	15.8	15.5	17.7	14.3	19.9	13.6	18.0	16.9	16.7	15.2	19.6	23.8	17.1	25.1	25.2	17.6	29.8	22.1	15.4	30.0	12.7	16.2	19.1

Values for V_T are given in mL/g, for K_1' in mL/g/min, and for k_2' in min^{-1}.

worldwide, with no requirement for an on-site cyclotron for positron-emitters, might provide some advantages, although the spatial resolution of SPECT systems is lower, and the quantitative accuracy of the SPECT data is poor compared with that of dedicated PET systems. Fourth, the satisfactory safety profile of this compound, with such a high specific activity, ensures that the administration dose of ^{123}I-5IA is well below the threshold at which pharmacologic effects first appear (*18–21,23,24*).

The quantitative analysis of ^{123}I-5IA was performed using a compartmental model. First, the 3-compartment model was chosen. This configuration might theoretically be a better choice for estimating the kinetic parameters for ^{123}I-5IA; however, the 4-parameter configuration could not provide goodness of fit for the present data—namely, it seemed that the ^{123}I-5IA in nonspecific and specific compartments mixed immediately. Therefore, 4-parameter kinetic analysis seemed to be an unsuitable choice for quantification of human nAChRs using ^{123}I-5IA SPECT. Thus, the quantitative V_T values in various regions of the human brain were estimated by 2-compartment model analysis. The 2-compartment model has a small number of parameters to be identified in the brain, making this choice simpler and acceptable for ^{123}I-5IA. This fact could be observed by the relatively stable performance of the estimated parameters using %COV (Table 1).

The V_T values from 2-compartment model analyses using the 6-h scan time showed the highest density of nAChRs in the thalamus; moderate density in the brain stem, basal ganglia, and cerebellum; and low density in the frontal, parietal, temporal, and occipital cortices. This distribution is compatible with the known distribution of nicotinic receptors in humans (*2*). A previous autoradiographic study using ^{3}H-epibatidine, which has similar affinity for the $\alpha_4\beta_2$ subtype of nAChR, described 3 levels of density of nAChRs in the human brain (high, moderate, and low) (*29*). The results of the present study are consistent with those for almost all regions evaluated in the study of Marutle et al. (*29*). Shimohama et al. (*10*) described the regional distribution of nAChRs in human brain using (−)-^{3}H-nicotine in an in vitro receptor assay study. The distribution volumes described for ^{123}I-5IA at 360 min after injection correlated well with the nAChR densities measured using (−)-^{3}H-nicotine (r^2 = 0.91) (Fig. 6), although there is some variation at the area with low density of nAChRs. Some divergence in the affinity of these compounds to the nAChR $\alpha_4\beta_2$ subtype, associated with some affinity toward other subunits in the brain, could explain these small differences (*15,29,30*). Thus, the possibility that ^{123}I-5IA binds with other mammalian nAChR subtypes cannot be excluded (*17,29,31*). In addition, significant losses or upregulation of nAChRs in the brain have been related to various situations, such as normal aging, neurodegenerative diseases, and tobacco use (*2,7–10,29*). In this context, ^{123}I-5IA will provide valuable information from living subjects in various clinical situations.

TABLE 4

^{123}I-5IA Parameter Estimates for 2-Compartment, 2-Parameter Model Analysis with 90-Minute Scan Time

Volunteer			Frontal cortex			Parietal cortex			Temporal cortex			Occipital cortex			Basal ganglia			Thalamus			Brain stem			Cerebellum		
No.	Sex	Age (y)	V_T	K_1'	k_2'	V_T	K_1'	k_2'	V_T	K_1'	k_2'	V_T	K_1'	k_2'	V_T	K_1'	k_2'	V_T	K_1'	k_2'	V_T	K_1'	k_2'	V_T	K_1'	k_2'
1	M	20	13.3	0.18	0.013	12.7	0.19	0.015	13.1	0.17	0.013	10.8	0.20	0.018	14.7	0.18	0.012	30.4	0.18	0.006	20.8	0.18	0.009	17.3	0.22	0.013
2	F	20	13.2	0.24	0.018	11.3	0.24	0.021	12.3	0.23	0.019	10.7	0.27	0.025	12.8	0.25	0.020	23.3	0.26	0.011	15.4	0.25	0.016	13.4	0.27	0.020
3	M	20	13.4	0.18	0.014	12.9	0.18	0.014	12.9	0.18	0.014	11.8	0.20	0.017	13.9	0.18	0.013	23.3	0.20	0.009	20.0	0.17	0.009	14.2	0.21	0.015
4	M	20	16.3	0.27	0.017	15.8	0.27	0.017	16.0	0.28	0.017	14.9	0.27	0.019	18.1	0.27	0.015	24.6	0.29	0.012	24.2	0.25	0.011	18.2	0.31	0.017
5	M	20	14.2	0.21	0.015	13.9	0.21	0.015	13.2	0.20	0.015	11.9	0.21	0.018	14.4	0.22	0.015	26.4	0.20	0.008	20.7	0.20	0.010	15.7	0.21	0.013
6	M	20	18.4	0.22	0.012	18.2	0.22	0.012	17.0	0.21	0.012	15.6	0.22	0.014	22.1	0.22	0.010	41.7	0.23	0.006	29.9	0.22	0.008	18.1	0.24	0.014
7	F	20	17.8	0.24	0.014	16.5	0.24	0.014	17.4	0.25	0.015	14.2	0.26	0.019	19.7	0.24	0.012	41.2	0.25	0.006	29.8	0.27	0.009	22.4	0.28	0.013
8	F	21	14.2	0.22	0.016	13.9	0.23	0.017	13.7	0.22	0.017	12.2	0.25	0.020	14.6	0.23	0.016	30.5	0.24	0.008	23.0	0.22	0.010	17.1	0.25	0.014
9	F	21	13.2	0.27	0.021	13.1	0.27	0.020	13.4	0.27	0.020	11.6	0.29	0.025	14.8	0.27	0.019	25.0	0.27	0.011	19.7	0.25	0.013	18.3	0.28	0.018
10	F	22	11.3	0.22	0.020	11.2	0.24	0.021	10.9	0.22	0.020	10.2	0.24	0.024	12.8	0.22	0.017	19.2	0.23	0.012	15.6	0.21	0.014	12.0	0.26	0.022
11	M	22	14.3	0.22	0.016	13.8	0.22	0.016	15.2	0.21	0.014	13.3	0.21	0.016	15.7	0.22	0.014	23.5	0.23	0.010	29.2	0.21	0.007	15.5	0.24	0.016
12	M	23	17.1	0.17	0.010	15.9	0.18	0.011	16.3	0.18	0.011	14.9	0.19	0.013	16.4	0.18	0.011	28.6	0.17	0.006	23.9	0.19	0.008	16.6	0.20	0.012
13	M	25	13.4	0.22	0.016	12.7	0.21	0.017	11.7	0.21	0.018	11.0	0.25	0.023	13.4	0.22	0.016	18.7	0.24	0.013	18.7	0.23	0.012	14.4	0.27	0.018
14	F	36	14.8	0.24	0.016	14.1	0.25	0.017	15.5	0.25	0.016	13.6	0.26	0.019	16.8	0.26	0.015	22.4	0.25	0.012	23.4	0.25	0.011	17.9	0.28	0.015
15	F	49	12.6	0.21	0.017	12.3	0.22	0.018	12.0	0.21	0.018	10.6	0.24	0.023	13.7	0.23	0.017	20.4	0.24	0.014	16.6	0.23	0.012	15.1	0.26	0.017
16	F	50	15.6	0.22	0.014	14.8	0.23	0.016	15.9	0.24	0.015	13.3	0.27	0.020	19.4	0.22	0.012	32.8	0.23	0.007	21.5	0.23	0.011	21.4	0.26	0.012
17	F	56	18.8	0.27	0.015	18.7	0.27	0.014	18.5	0.28	0.015	15.5	0.29	0.019	20.6	0.25	0.012	33.8	0.28	0.008	24.9	0.27	0.011	22.7	0.33	0.015
18	M	59	10.4	0.21	0.020	10.8	0.21	0.020	10.4	0.23	0.022	9.9	0.25	0.025	11.7	0.21	0.018	17.0	0.22	0.013	15.7	0.23	0.015	12.4	0.26	0.020
19	M	59	15.9	0.20	0.013	13.5	0.18	0.014	14.8	0.19	0.013	12.5	0.20	0.016	16.1	0.20	0.012	23.4	0.19	0.008	17.5	0.19	0.011	16.3	0.20	0.012
20	F	61	13.7	0.20	0.014	13.4	0.21	0.016	13.1	0.21	0.016	11.8	0.21	0.018	16.2	0.20	0.012	26.4	0.20	0.008	22.1	0.20	0.009	15.9	0.22	0.014
21	M	71	14.4	0.20	0.014	12.8	0.21	0.017	12.7	0.22	0.017	12.0	0.23	0.019	15.1	0.21	0.014	22.0	0.23	0.011	17.1	0.21	0.012	17.5	0.28	0.016
All																										
Mean			14.6	0.22	0.015	13.9	0.22	0.016	14.1	0.22	0.016	12.5	0.24	0.020	15.8	0.22	0.014	26.4	0.23	0.009	21.4	0.22	0.011	16.8	0.25	0.015
SD			2.2	0.03	0.003	2.1	0.03	0.003	2.2	0.03	0.003	1.8	0.03	0.004	2.8	0.03	0.003	6.7	0.03	0.003	4.5	0.03	0.002	2.9	0.04	0.003
%COV			15.1	13.1	17.7	15.2	12.0	16.9	15.7	13.6	17.6	14.1	13.3	18.0	17.4	12.5	18.7	25.4	13.5	27.5	21.1	12.6	22.1	17.3	14.0	18.6

Values for V_T are given in mL/g, for K_1' in mL/g/min, and for k_2' in min^{-1}.

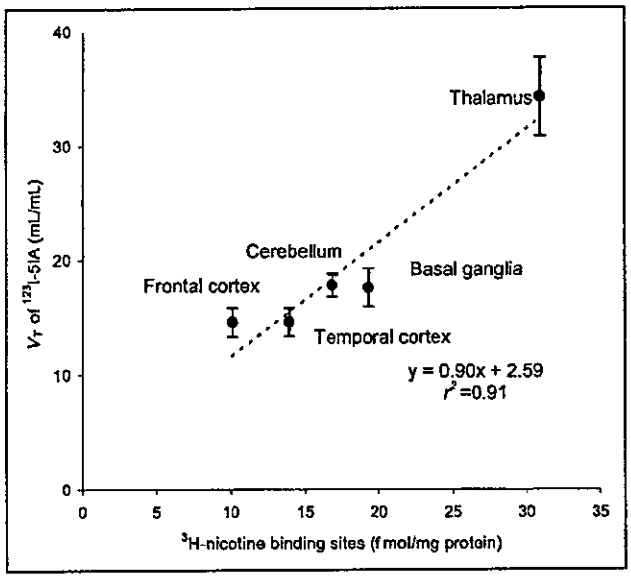

FIGURE 6. Correlation between distribution volumes described for ^{123}I-5IA at 360 min after injection with those specific bindings for (−)-^{3}H-nicotine in postmortem study (r^2 = 0.91) (*10*).

Furthermore, although the density of the $\alpha_4\beta_2$ subtype of nAChR in the cerebellum was lower in animals, a substantial presence was found in the human brain (*2*). Therefore, the cerebellum is an inappropriate reference region in quantitative studies using ^{123}I-5IA in humans. The study also indicated that there is no other receptor-poor region that is appropriate as a reference region for SPECT (*2*). Thus, use of the reference region is not applicable to the quantification of nAChR in the human brain.

In the present study, the rate parameter constant K_1' showed relative low values (0.25 ± 0.04 in cerebellum at 90-min scan time, Table 4). The K_1' represents the delivery rate constant from the plasma to the tissue compartment (C_{f+ns+s}), and it is basically driven by the regional cerebral blood flow (F) and the single-pass extraction fraction of the ligand into the brain (E_0). Considering that the cerebral blood flow is normal in the groups of subjects, the extraction fraction of ^{123}I-5IA might be the reason for these lower values. Saji et al. (*18*) showed in an animal study that ^{123}I-5IA has a moderate brain uptake index (BUI = 31 ± 6), which was lower than that of nicotine (BUI = 103 ± 12). These findings are in complete agreement with our results.

Besides the simplicity of the method and the independency of the model configuration of the tissue compartment, the application of graphical analysis for determination of distribution volumes (V_{LG}') in receptor binding studies offers greater accuracy. The main outcome from this method of measurement can be estimated with much higher accuracy than individual parameters of radioligand kinetics (*32*). In the present study, the highest slopes correlated with those regions with higher densities of nAChRs in the human brain using ^{123}I-5IA SPECT (*2*). The analysis of the correlation between V_T' and V_{LG}' values showed good agreement (r^2 = 0.99) (Fig. 7) as well as between the transfer constant K_1' and K^*_1 (r^2 = 0.96) ($P < 0.01$, for both). The results indicate that the graphical method showed essentially the same information of measurement of nAChRs using ^{123}I-5IA SPECT with acceptable accuracy.

Taking account of all factors that determine the V_T' values of ^{123}I-5IA in the present study, 2 independent variables were identified: regions in the brain and length of data acquisition. The variable subject was not considered due to the uniform population evaluated in this study (age of subjects around 20 y in group 1 subjects). The variability of receptor densities and metabolism of ^{123}I-5IA should be quite small in such a uniform population, and distribution volumes would be successfully estimated from data of a short scan time because biases caused by short data should be similar in all subjects. Thus, a factorial ANOVA was applied considering all factors together. The results showed that the length of the scan was not critical to determining the distribution volume in different brain regions. The factor region in the brain was significant and this finding can be easily explained by the differences in the V_T' values between those regions in the brain. Once both factors interacted as a single term (region length), the results showed no statistical significance, so the region and length effects can be assumed to be consistent across levels of the other factor. Therefore, a short scan time (i.e., 90-min) can be used to evaluate the distribution volume in human brain using ^{123}I-5IA.

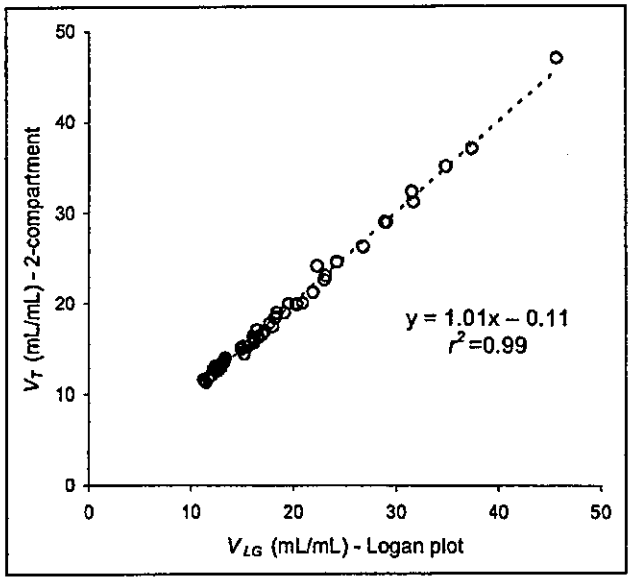

FIGURE 7. Analysis of correlation between distribution volumes from compartmental model (V_T) and graphical analyses (V_{LG}) performed during 360-min scan time. Circles represent V_T and V_{LG} values in various brain regions analyzed from all subjects in first group of volunteers. V_T and V_{LG} values from 2-compartment model and Logan plot analyses demonstrated high correlation index (r^2 = 0.99) ($P < 0.01$).